Building a random forest machine learning model for annual Net Ecosystem Exchange estimation in agricultural fields using discontinuous atmospheric Eddy Covariance measurements.

Camille Pery[1,2,3], Pierre Polsenaere[1], Eric Lamaud[2], Natacha Volto[4], Nathalie Long[4], Jonathan Deborde[1], Shunko Bolsée[2], Olivier Philippine[5], Vona Méléder[6,7], Christine Dupuy[4]

[1] Ifremer, COAST, 17390 La Tremblade, France
[2] INRAe, ISPA, 33140 Villenave D'Ornon, France
[3] Univ. Bordeaux, CNRS, Bordeaux INP, UMR 5805, F-33600 Pessac, France
[4] LIENSs, UMR7266 CNRS- La Rochelle Université, 17000 La Rochelle, France
[5] Unima, 17180 Périgny, France
[6] Nantes Université, ISOMer, 44000 Nantes, France
[7] Institut Universitaire de France, IUF, France

Correspondence to: Camille Pery (camille.pery@bordeaux-inp.fr)

Abstract. Atmospheric CO_2 exchanges in agroecosystems are strongly controlled by plant phenology, management and microclimatic conditions; yet obtaining finely resolved flux estimates across heterogeneous agricultural landscapes remains challenging. This study evaluates the ability of a single Eddy Covariance (EC) system combined with wind-sector partitioning and Random Forest (RF) modelling to estimate the annual Net Ecosystem Exchange (NEE) of adjacent fields (wheat, mixed-grain, permanent grassland) in the Marais poitevin wetland (French Atlantic coast). Fluxes were measured over the period 2023/02/01 – 2024/01/31 and attributed to eight wind sectors, each used as a proxy for the corresponding field or landscape feature that dominates its footprint. Two modelling strategies were compared (i) a single global RF trained on all sectors and (ii) sector-specific RFs trained separately for each wind sector. RF models globally showed good overall performance ($R^2 \approx$ 0.20-0.94 depending on sector and period), but this apparent equivalence broke down once fluxes were reconstructed over the full annual cycle: the sector-specific approach then better reproduced phenological dynamics and management-driven flux reversals (harvest, senescence) than the global model, which compressed inter-sector variability by up to 67%. Annual NEE estimated from the sector-specific models indicated that the mixed-grain field acted as net source (+151 g C m^{-2} yr^{-1}), whereas the permanent grassland and the wheat field acted as net sinks (−145 and −308 g C m^{-2} yr^{-1}, respectively). A light-response-curve partitioning of these reconstructed fluxes into gross primary production (GPP) and ecosystem respiration (Reco) revealed contrasting phenological signatures behind different land-cover. Methodology and associated limitations/uncertainties due to flux measurement and modelling, footprint attribution and sector delineation, and the limited one-year observation period are particularly addressed. This study highlights the novelty and practical value of coupling a single EC system with wind-sector partitioning and machine learning approaches to resolve carbon fluxes at the field scale within heterogeneous agricultural landscapes. This integrated approach provides an alternative to traditional multi-tower setups, offering new opportunities to monitor spatial carbon dynamics and management effects in real agricultural mosaics. Beyond methodological innovation, this

work provides one of the first field-scale, uncertainty-resolved carbon flux datasets for a mosaic of contrasting agricultural land covers monitored by a single EC tower, offering a transferable framework to better constrain the terrestrial carbon balance of retro-littoral wet and agricultural landscapes.

Keywords: Eddy Covariance, Random Forest, Net Ecosystem Exchange, wind sectors, agriculture, gap-filling.

1 Introduction

Agricultural lands cover a vast fraction of the terrestrial biosphere with around 50% of the Earth's vegetated land surface (about 5 billion ha) under cultivation, grassland or rangeland; this extensive area makes agroecosystems a major component of the global carbon cycle. Indeed, since 1750 corresponding to the start of the industrial era, conversion of forests and meadows to cropland and grassland has released large amounts of CO_2 on the order of 214 ± 67 PgC from biomass and soils, contributing roughly to a quarter of anthropogenic greenhouse-gas emissions (Zomer et al., 2017). In the last decade, net CO_2 emissions from land-use change (mostly driven by agriculture) averaged about 4.2 ± 2.6 Gt CO_2 yr^{-1} (Friedlingstein et al., 2025). At the same time, agricultural ecosystems can remove atmospheric CO_2 through crop photosynthesis and store part of this carbon in plant biomass and soils. However, their overall role as a carbon sink or source depends also largely on agricultural management practices. Conventional practices, such as intensive tillage and crop residue removal, can reduce soil carbon stocks and increase greenhouse gas emissions, whereas more conservational practices can enhance soil carbon sequestration and mitigate CO_2 emissions. Globally, agricultural soils hold on the order of 8-10% of the world's soil organic carbon (Wu et al., 2024), so even small changes in land management can have measurable impacts on the atmospheric CO_2 concentration. Climate and land-use intensity control the Net Ecosystem Exchange (NEE) of agroecosystems in complex and interconnected ways: solar radiation and air temperature are the primary drivers of gross primary production (GPP) in many temperate croplands (Moreaux et al., 2020), while water availability, plant phenology and vapor pressure deficit (VPD) modulate the growing-season uptake. Crop type and anthropogenic management (e.g., fertilization, irrigation, harvest) further alter the balance between photosynthesis and respiration; for instance, deep-rooted or perennial crops typically achieve higher seasonal carbon uptake than shallow-rooted annuals, and no-harvest practices slow down soil CO_2 release (Bajgain et al., 2018). . Thus, the net ecosystem carbon exchange of agricultural fields sensitively depends on crop species, phenological stage, and local environment variables, as well as on socio-economic factors determining land-use intensity (Moreaux et al., 2020; Zomer et al., 2017).

To quantify NEE over large spatial scales and fine time resolution, the Eddy Covariance (EC) technique has become a widely used method in ecosystem science, although it remains costly and technically demanding. EC deploys fast response anemometers and CO_2/H_2O Infra-Red Gas Analysers (IRGA) on towers to directly measure the turbulent flux of CO_2 between the biosphere and atmosphere (Baldocchi, 2020). Since the late 1990s, global networks of EC towers (e.g. FLUXNET, AmeriFlux, AsiaFlux, ICOS, etc.) have accumulated long time series of carbon and water fluxes from hundreds of sites

representing diverse biomes (Baldocchi, 2020). In Europe, the Integrated Carbon Observation System (ICOS) network similarly provides standardized CO_2 flux measurements through 180 stations deployed across 16 European countries. In total, these networks have been invaluable for linking ecosystem carbon exchange to climate drivers; they include sites across continents (North America, Europe, Asia, Africa, etc.) and ecosystem types from boreal and temperate forests to grasslands, croplands, wetlands, and even urban landscapes. Baldocchi (2020) notes that adding new towers to these EC networks has not significantly changed the aggregate flux statistics despite extending coverage into new regions; however, that global EC networks are not free of representativeness bias, as several biome types (e.g., subtropical and dry regions, mountainous forests, wetlands) remain under represented, and new towers may disproportionately cover already well-represented biomes. Despite these coverage gaps, the accumulated multi-decadal observations have elucidated several key environmental controls on ecosystem carbon cycling. Solar radiation emerges as the primary driver of photosynthetic carbon uptake, with light response curves showing saturation effects at high irradiance levels and demonstrating how different vegetation types exhibit varying light-use efficiencies (Reichstein et al., 2007; Wohlfahrt and Gu, 2015). Temperature controls operate through multiple pathways: while moderate warming generally enhances both photosynthesis and respiration, the temperature sensitivity of respiration, commonly expressed as the Q_{10} coefficient (i.e., the factor by which a biological process increases for a 10 °C rise in temperature), typically exceeds that of photosynthesis, leading to reduced net carbon uptake at higher temperatures (Kirschbaum, 1995; Lloyd and Taylor, 1994; Mahecha et al., 2010). Moisture availability represents another fundamental control, with VPD strongly regulating stomatal conductance and thus photosynthetic rates, while soil water content directly affects both plant productivity and microbial respiration (Knauer et al., 2018; Novick et al., 2016).

EC measurements also have well-known limitations; for instance, raw flux time series typically contain gaps due to instrument maintenance, meteorological conditions (precipitation), low turbulence or filtering of spurious data. Then, filling these gaps is necessary, requiring statistical or machine-learning gap-filling routines, which can at the same time, introduce uncertainty if large or systematic gaps occur (Gao et al., 2023). Moreover, an EC tower integrates fluxes over an upwind footprint whose size and shape change with surface roughness, atmospheric stability and wind direction; in heterogeneous landscapes, a single tower may sample multiple land covers, complicating attribution of fluxes to specific fields or vegetation types. Such footprint heterogeneity can bias estimates when land cover is patchy, a particular concern for small agricultural fields in a mosaic of crops and fallows (Kumari et al., 2020; Bou-Zeid et al., 2020).

Recently, Machine Learning (ML) techniques have been increasingly applied to model and gap-fill NEE, taking advantage of large EC datasets and remote-sensing/meteorological inputs. Unlike simple empirical regressions or process-based models that require detailed parameterization, ML methods can capture complex nonlinear interactions without explicit mechanistic assumptions. Typical algorithms include Random Forests (RF), artificial neural networks, support vector machines, and ensemble approaches. For example, Zeng et al. (2020) used a RF model to upscale EC-based NEE, GPP and R_{eco} from FLUXNET datasets across the globe, producing high-resolution carbon flux maps. In agricultural contexts, ML has proven

effective for both gap-filling and predictive modelling. Gao et al. (2023) demonstrated that a RF-based gap-filling framework (combined with moving-average decomposition) outperformed conventional methods (including linear interpolation, mean diurnal variation, and look-up table approaches commonly used in the FLUXNET standardized processing) over extended CO_2 flux gaps. A recent study applied a knowledge-guided ML framework to agroecosystems in the U.S. Corn Belt and showed it surpassed both pure process models and "black-box" ML models in quantifying carbon dynamics (Liu et al., 2024). These studies highlight key advantages of ML, i.e., flexibility in assimilating diverse inputs (weather, soil moisture, phenology, management) and the ability to identify subtle patterns in flux variability. In practice, RF are especially popular for flux prediction because they are robust to overfitting and provide variable importance metrics.

In this context, the La Rochelle Zero Carbon Territory (LRTZC) project (2019-2027) provides a regional framework for carbon monitoring and mitigation in the perimeter of La Rochelle Agglomeration. The project has pledged carbon neutrality by 2040 through combined mitigation and sequestration efforts. Under LRTZC, the Blue Carbon axis and associated research actions target carbon fluxes in coastal ("blue carbon") and retro-littoral ecosystems that correspond to freshwater, brackish and salt shallow systems separated from tidal immersion by dykes and locks, and are now numerous particularly along the French Atlantic coast. As part of these efforts, an EC tower has been deployed from February 2023 to February 2024 in a rural wetland (freshwater marsh, Marans) to monitor retro-littoral NEE. This wetland ecosystem is constituted by agricultural parcels (terrestrial compartment) separated by ditches (aquatic compartment). Because the EC system cannot fully isolate fluxes from the water ditches, this single tower overlooks three adjacent fields with different crops and management histories. By partitioning the 360° EC data into specific chosen wind-direction sectors, the "wind-sector approach" adopted in the present study allows analysing separate NEE time series for each parcel of interest depending on wind directions.

The objective of this study was to estimate the NEE of the three individual fields from EC data partitioned into wind sectors, each sector being used as a proxy for the corresponding field or landscape feature, that dominates its footprint. RF models were built for each wind sector to predict CO_2 flux from meteorological and soil variables measured at the tower location. Annual NEE was then computed for each field. NEE was further partitioned into GPP and Reco for each sector, using a light-response-curve approach applied to daytime NEE, in order to quantify the relative contribution of photosynthetic uptake and respiration to each field's annual carbon NEE. To test the benefit of this disaggregated approach, a "pooled" model was trained using all data from all sectors (ignoring field boundaries), and its flux predictions were compared to those obtained from the separate specific models. The hypothesis was that sector-specific models would more accurately capture each field's distinct NEE (reflecting crop and management differences) and thus yield more precise values than a single model that pooled all fields. By evaluating disaggregated versus pooled modelling, the study aimed to demonstrate how wind-sector partitioning could enhance carbon monitoring in heterogeneous agricultural landscapes. In this way, complete annual NEE values of neighbouring fields could be compared under the same climatic conditions without multiple tower needs.

2 Materials and methods

2.1 Study site

The study was conducted in the city of Marans, located in the Charente-Maritime department in southwestern France (46.31° N, 0.99° W). Charente-Maritime is characterized by a temperate oceanic climate and a predominantly agricultural landscape representing 62% of the total Charente-Maritime surface, corresponding to 425,267 ha; the regional land use is dominated by cereal crops (63% of the utilised agricultural area, UAA), followed by permanent grasslands (18%), alongside viticulture and livestock farming (Agreste, 2020).

The experimental site comprises three adjacent land fields representative of the regional land use structure. To the northeast, a field was cultivated with mixed grain (cereals and legumes), sown in autumn and harvested on 24th May 2023, after which the field remained as bare soil until it was re-sown with mixed grain in autumn 2023. To the south, a second field was planted with wheat in February and harvested on 7th July 2023, after which it remained as bare soil for the remainder of the measurement period. In the northwest, a permanent grassland field, continuously grazed by cattle from June to November (i.e., cattle numbers of 10 in February 2023, 41 in April 2023 and 43 in July 2023), was maintained throughout the study. Each field is delineated by hydrological features, including a network of drainage ditches typical of the Marais poitevin wetland system (Butzer, 2002). The Brune Ditch runs between the northern fields and the wheat field and is intersected by a smaller secondary ditch bordered by sparse woody vegetation separating the mixed grain and grassland fields (Fig. 1).



Figure 1. Agricultural fields located in the Poitevin Marsh (Marans city) seen by the Eddy Covariance station (red dot) deployed from February 2023 to February 2024. Wheat field in the south, mixed-grain field in the northeast and grassland in the northwest sectors (Drone orthomosaic image taken in February 2023). The Brune Ditch (in brown) orientated from west to east, separates wheat fields in the south from mixed-grain and grassland fields in the north.

The EC tower was installed on the 1st of February 2023 at a narrow-grassed strip approx. 5 m wide adjacent to the Brune Ditch, providing a central location from which flux measurements could be made across the multiple land covers. The site configuration allowed for the assessment of NEE across contrasting land uses within a complex agricultural landscape.

2.2 Atmospheric CO_2 exchanges and associated meteorological data measured at the ecosystem scale by Eddy Covariance method

2.2.1 Eddy Covariance data acquisition

The EC technique is a micrometeorological method that quantifies net CO_2 fluxes at the ecosystem-atmosphere interface. In the atmosphere, CO_2 is transported by numerous eddies of varying size and frequency which occur in the surface boundary layer. The EC method relies on measuring the covariance between fluctuations in vertical wind velocity and scalar concentrations within these eddies. The CO_2 flux can be expressed as:

$$F = \overline{\rho_d w s} \approx \overline{\rho_d w' s'}$$

where the overbar indicates the time averaging and the prime represents fluctuations around this average (Burba, 2013; Reynolds, 1886). Here, (ρ_d) denotes the dry air density (kg m^{-3}), (w) the vertical wind velocity (m s^{-1}), and (s) the dry mole fraction of CO_2 (mol mol^{-1}, commonly expressed in µmol mol^{-1} or ppm). The covariance between these variables yields a mass flux with units of kg m^{-2} s^{-1}. For CO_2 exchange studies, this mass flux is converted into a molar flux by dividing by the molar mass of CO_2 (MCO_2 = 44.01 g mol^{-1}) and is therefore commonly reported in µmol m^{-2} s^{-1}. Negative CO_2 flux values indicate the ecosystem acts as a CO_2 sink, while positive flux values indicate ecosystem source behaviour.

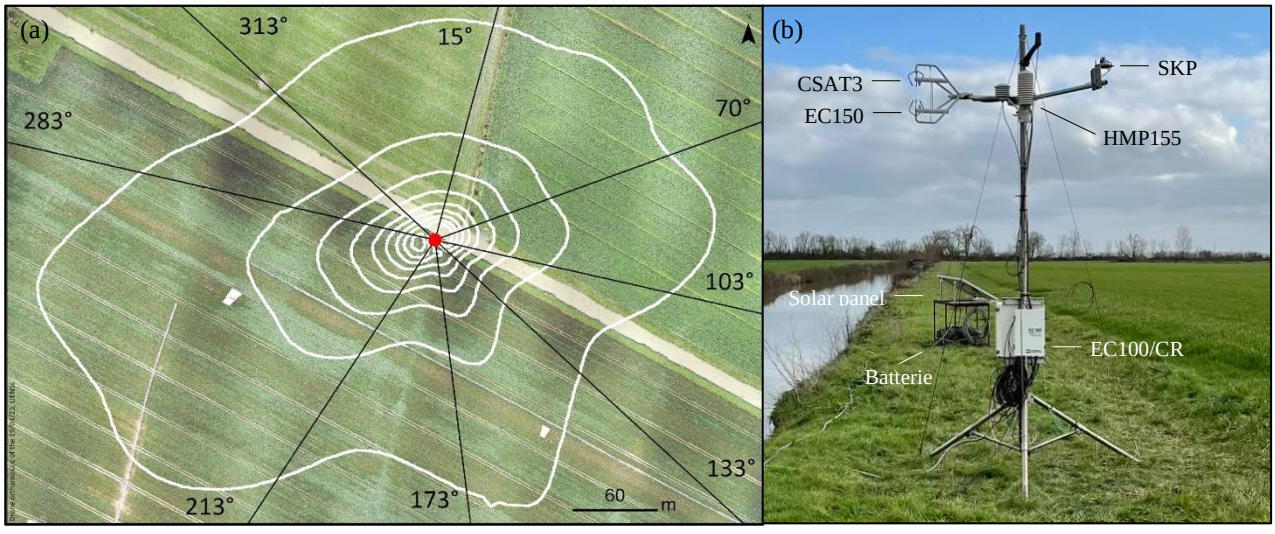


Figure 2. (a) Study site spatial partitioning into wind direction sectors for footprint-based attribution of CO_2 flux measurements to land cover types. High-resolution drone orthomosaic of the study area showing angular sectors centred on the EC tower (red dot). 15° to 70°: Sector 1 (hybrid transition zone), 70° to 103°: Sector 2 (mixed grain), 103° to 133°: Sector 3 (ditch), 133° to 283°: Sectors 4, 5 and 6 (wheat), 283° to 313°: Sector 7 (ditch), and 313° to 15°: Sector 8 (grassland). 10% to 90% contour lines in white of the annual footprint are shown. (b) The atmospheric EC station set-up with the two main anemometer and CO_2 EC sensors (CSAT3A and EC150, Campbell Scientific) linked to EC100 electronics module connected to the data acquisition central (CR6), with the associated environmental sensors (HMP155A, SKP 215 and TE525MM). The system is powered by batteries charged by solar panels (see main text for more details).

Mean fluxes were calculated over a 10 min averaging time period, as particularly adapted for more coastal and dynamic systems such as wetlands (present study), salt marshes (i.e., Mayen et al., 2024) and tidal flats (i.e., Polsenaere et al., 2012). To justify the 10-min averaging period instead of the usual 30, comparisons were done between the mean of the three 10 min values and the corresponding mean values obtained with an averaging time period of 30 min (see graphs in Appendix A, Fig. A1); these later showed no low frequency losses on the 10 min flux data, though some dispersion between both 10 min and 30 min mean values (u^*, wind speeds, mean fluxes) were noticed. Choosing a 10 min averaging time period (instead of 30 min) permitted losing less data due to non-stationary conditions and/or electronical noises leading to potential and more data suppression (with the 30 min choice) according to our data quality check procedure adopted here (see Appendix A, Fig. A1 and detailed procedure below in Section 2.2.2).

The EC station (Campbell Scientific, Logan Utah), installed and monitored from February, 1st 2023 to February, 1st 2024 between three agricultural fields (Fig. 1), included the following sensors positioned at the top of a 3m tower mast (Fig. 2b): an ultrasonic anemometer (CSAT3A) that measures three-dimensional wind speed components, and an open-path IRGA (EC150, connected to the EC100 module) that measures CO_2 and H_2O concentrations in the air both at a frequency of 20 Hz. The station also included additional sensors measuring various environmental parameters every 10-min: a photosynthetically active radiation (PAR) sensor (SKP215), an air temperature and relative humidity sensor (HMP155A), and a rainfall sensor (TE525MM, Texas Electronics) positioned few meters away in front of the tower. Soil temperature and water content were measured by another probe (CS655). The data acquisition system was powered by two batteries (12 volts, 260 Ah) charged by monocrystalline solar panels (24 V, 200Wp module with MPPT 100 V/30 A controller; Victron Energy). High-frequency data were recorded on an SD micro-card and replaced every two weeks along sensor cleaning. Meteorological data were stored in the central acquisition system (CR6 datalogger, Campbell Scientific) (Fig. 2b).

2.2.2 EC data processing and filtering

Raw EC data were processed using the EddyPro software (EddyPro® v7.0.8, LI-COR Inc.). Following Vickers and Mahrt (1997) the processing included several key steps: (1) unit conversion to check that the units for instantaneous data are appropriate and consistent to avoid any errors in the calculation and correction of CO_2 fluxes; (2) despiking to remove outliers in the instantaneous data from the anemometer and gas analyser due to electronic and physical noise and replaced the detected spikes with a linear interpolation of the neighbouring values; (3) amplitude resolution to identify situations in which the signal variance is too low with respect to the instrumental resolution; (4) double coordinate rotation to align the x axis of the

anemometer to the current mean streamlines, nullifying the vertical and cross-wind components; (5) time delay removal by detecting discontinuities and time shifts in the signal acquisition from the anemometer and gas analyser (i.e. covariance maximization option for the time lag detection method that calculates the most likely time lag based on the circular correlation procedure to avoid possible flux underestimations in the case of existing potential time lags); (6) detrending with removal of short-term linear trends to suppress the impact of low-frequency air movements; and (7) performing the Webb-Pearman-Leuning (WPL) correction to take into account the effects of temperature and water vapor fluctuations on the measured fluctuations in the CO_2 and H_2O densities (Burba, 2013).

For detrending, fluctuations were calculated as deviations from a linear trend over each averaging period (Gash and Culf, 1996). Data with more than 10% missing high-frequency observations were excluded, leaving 4% missing values in the EddyPro outputs. Additional extreme values were further identified and removed using the median absolute deviation (MAD) method (Papale et al., 2006). The MAD was calculated over a 2-week mowing window, separately for daytime and night-time periods and values above 5.2×MAD were removed. Without extreme values, the number of missing values reaches 12% for the studied period from 2023-02-01 to 2024-01-31. Then, the data were filtered to remove periods corresponding to friction velocity (u_*) values below 0.1 m s^{-1}. This parameter quantifies atmospheric turbulence and is used to identify poorly mixed periods. Under stable atmospheric conditions, the EC method may underestimate fluxes because the air near the ground can become decoupled from the air above; this can result in CO_2 accumulation that is not fully captured by the measurements (Barr et al., 2013; Gu et al., 2005). This u_* filter improves the reliability of EC measurements particularly done at night. After this filtering step, 32% of the CO_2 flux data were missing. Of the filtered data, 23% corresponded to nighttime periods, compared to 9% during the daytime (for more detail, see Mayen et al., 2024; 2025). At last, to remove extreme values particularly during the November 2023 storm event (Sect. 3.1), we applied additional hard limits based on the observed range of physiologically realistic ecosystem fluxes. During this storm event, transient flow distortion and non-stationary turbulence generated flux spikes that were considered instrumentally implausible rather than representative of realistic ecosystem responses. The hard limits also accounted for changes in crop management and ecosystem activity. Before harvest, NEE values were constrained between +20 and −50 μmol m^{-2} s^{-1}, whereas after harvest, when ecosystem activity was substantially reduced, a range of +10 to −10 μmol m^{-2} s^{-1} was applied. These limits removed a small number of spurious observations, including the most extreme values associated with the November storm period in particular (Fig 3). After application of this additional hard-limits filter, the overall proportion of missing CO_2 flux data increased to 34% for the studied period.

The filtering procedure described above was applied exclusively to CO_2 flux measurements and did not affect the meteorological variables used as predictors in the random forest (RF) models. Missing data were minimal for these variables (mainly due to electronical noise and/or power supply), with approximately 0.03% for air and soil temperature and soil humidity, 0.005% for relative humidity, and 0.68% for wind direction, wind speed and atmospheric pressure. No gap exceeded seven consecutive missing observations (70 min) and given their limited extent and short duration, these gaps were filled using a simple mean-based approach to ensure temporal continuity in the meteorological inputs.

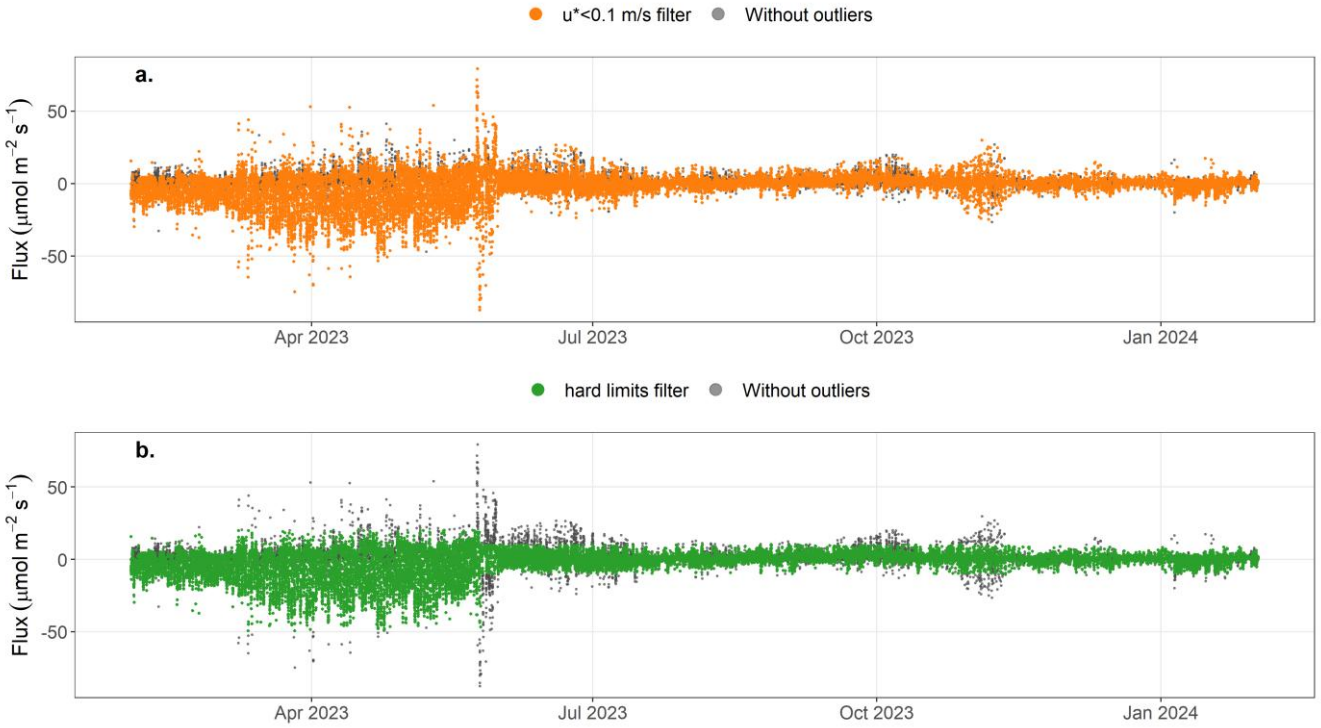


Figure 3. Comparison of NEE time series after application of (a) the u_* (< 0.1 m s^{-1}) filter and (b) the hard-limits filter. Grey points represent the dataset after outlier removal only, while coloured (orange and green) points indicate the retained fluxes after each filtering step (u_* and hard-limits filters, respectively). Missing data reached 32% after the u_* filter alone and 34.25% after the additional hard-limits filter (see Sect. 2.2.2).

2.3 Intermittent EC data modelling

2.3.1 Landscape-based wind sector classification, vegetation dynamic analysis and footprint estimation

To spatially constrain the different surface sources contributing to the measured NEE, we delineated a set of wind sectors that reflect both the surrounding land-cover distribution (Fig. 2a) and the roughness-related flow heterogeneity inferred from turbulence measurements (Fig. 4). The objective of the sectorisation was primarily to characterize the spatial heterogeneity of the flux footprint and the effects of contrasting management practices within the study area. In addition to the spatial analysis of landscape structure, we used the ratio between friction velocity (u_*) and mean wind speed (U) as a function of wind direction. Because u_* responds sensitively to upwind vegetation height, discontinuities and surface roughness, directional variations in the u_*/U ratio provide an empirical signature of surface-roughness transitions, making it possible to identify the position of ditch banks, riparian vegetation or flow disturbances induced by the tower infrastructure (Bolsée et al., 2026). Indeed, in the atmospheric surface layer, the presence of relief elements, whether they are plant-based as in our case or man-made, causes an increase in surface roughness (z_0), which leads to an increase in the roughness coefficient u_*/U, as inferred from the following equation $u(z) = (u_*/k)\ \ln((z - d)/z_0)$. Therefore, the spatial distribution of u_*/U, obtained from momentum EC flux

measurements allows differentiating the areas responsible for the CO_2 fluxes measured by the same set-up (Bolsée et al., 2026). In the present study, this approach was particularly effective after harvest, when all cropped fields were essentially bare soil while riparian corridors remained vegetated, thereby amplifying roughness contrasts between fields and allowing a precise alignment between directional u_*/U features and landscape elements. The spatial origin of the measured NEE was determined under all atmospheric stability conditions (instead of selecting only neutral conditions); indeed, it could give a biased view of the sectors where CO_2 fluxes come from, R_{eco} being linked to stable night-time conditions and GPP being the main component of daytime NEE under unstable conditions.

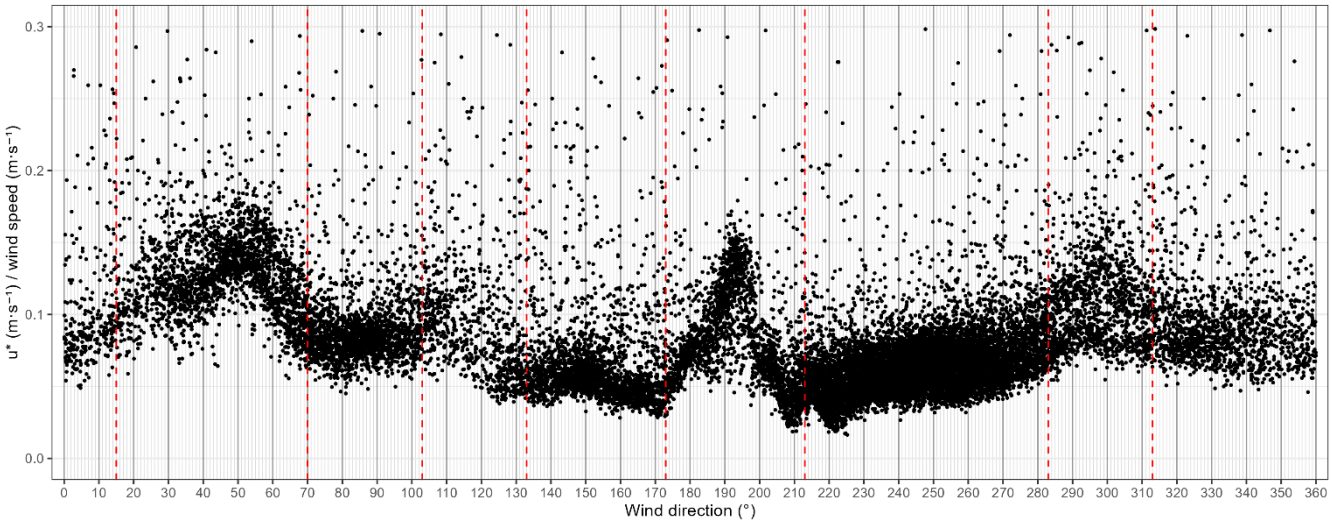


Figure 4. Directional variability of the u_*/U ratio after wheat harvest (10/07/2023), highlighting roughness transitions and disturbances used to define wind-sector boundaries (defined by dashed red lines) around the EC tower.

Based on the combined interpretation of land-cover maps and directional u_*/U patterns, the area surrounding the EC tower was partitioned into eight directional sectors reflecting the main land-cover units within the flux footprint (Figs. 2a and 4). Sector 1 (15–70°) corresponds to the transition zone between grassland and mixed-grain fields, together with the associated riparian vegetation. Sector 2 (70–103°) covers the mixed-grain field, up to the first ditch axis. Sector 3 (103–133°) isolates this first ditch and its bordering riparian corridor. The wheat field, extending from 133° to 283°, was further subdivided into three sub-sectors: Sector 4 (133–173°), Sector 5 (173–213°) and Sector 6 (213–283°), the combination of which (Sectors 4+5+6) reproduces the full wheat sector (133–283°). Sector 7 (283–313°) corresponds to the second part of ditch, centred around ~298°, and its riparian margin. Finally, Sector 8 (313–15°) corresponds to the permanent grassland. Sector 5 is centred on the wake of the sonic anemometer, whose peak is visible at 193° (Fig. 4). Although this wake does not directly bias CO_2 fluxes, it locally distorts the wind field in a way that renders the standard u_* filter (< 0.1 m s^{-1}) unreliable within this directional range. Throughout the manuscript, a distinction is clearly made between fields and sectors. The field (wheat, mixed grain or permanent grassland) is the management unit for which the annual NEE is sought, whereas the wind sector is the unit of analysis, i.e., the range of wind directions over which the flux footprint is dominated by the given corresponding land cover.

A sector is therefore a proxy for a field rather than the field itself, and the extent to which its fluxes can be interpreted as a field-scale NEE depends on the homogeneity of its footprint (Sects. 3.3 and 4.2). Three sets of sectors were then used to estimate the field budgets: Sectors 4, 5 and 6, individually and combined (Sectors 4+5+6), for the wheat field, Sector 8 for the permanent grassland and Sector 2 for the mixed-grain field. The remaining sectors were diagnostic: Sector 1 sampled the transition zone between the grassland and mixed-grain fields, and Sectors 3 and 7 the two ditch corridors.

Retaining all eight sectors, was necessary to reduce the imbalance in sample size across sectors and sub-periods: as shown by the associated number of 10-min observations (Table 1), the eight-sector scheme, together with the pre-/post-harvest temporal split, yields sub-groups ranging from a few hundred to several thousand observations, a spread that a coarser classification would only widen further. In particular, subdividing the wide wheat sector (133–283°) into three narrower sub-sectors (Sectors 4, 5 and 6) allows each of them to be sampled with a comparable, wind-direction-driven density of observations, avoiding a single, very large wheat class from dominating the dataset relative to the smaller mixed-grain, hybrid and ditch sectors (Table 1); this subdivision also makes it possible to assess whether the wheat field behaves consistently across its angular extent, or whether spatial heterogeneity remains within a single, apparently homogeneous field. Sectors 3 and 7 (the two ditch/riparian corridors) were retained for a similar diagnostic purpose: rather than providing a stand-alone NEE estimate for the ditches themselves, they serve as a point of comparison for the neighbouring mixed-grain (Sector 2) and grassland (Sector 8) sectors, helping to assess the extent to which riparian and open-water surfaces may contribute to, or "contaminate," the flux signal nominally attributed to these two crop and grassland sectors (see Sect. 3.3, 4.2).

In the present study, the footprint (Fig. 2a) was estimated with the Kljun et al. (2015) model and calculated using the constant measurement height (Zm=3m), the constant displacement height (d = 0.1 m), mean wind velocities, standard deviations of the lateral velocity fluctuations after rotation, the Obukhov length (L), friction velocities (u_*) and wind directions, measured by the station from February, 1st 2023 to 31st January 2024. No further specific parametrization, such as aerodynamic canopy height (Chu et al., 2018) was performed, as the averaged footprint we present was considered sufficient to our modelling approach. Footprint model distance outputs using Kljun et al. (2004) and Kormann and Meixner (2001) footprint models given by EddyPro, were also checked to help estimate whether the ditch's contribution was negligible or not.

NDVI time series were derived from 26 MODIS MOD13Q1.061 Vegetation Indices 16-Day composite products (Didan, 2021) (Terra platform, 250 m spatial resolution, tile h17v04), covering the period from 1st January 2023 to 31st January 2024 and obtained from the NASA Land Processes Distributed Active Archive Center (LP DAAC) via the NASA Earthdata Search portal. To analyse and better understand vegetation dynamics according to phenology and agricultural management, three well-defined, single-crop ("pure") agricultural fields were delineated, and for each of them, a single NDVI (normalized difference vegetation index) value per date was computed as the spatial mean of all MODIS pixels falling within the corresponding polygon, thereby representing the vegetation status of the parcel as a whole. Riparian vegetation located along the two canals as part of the EC footprint in certain sectors was explicitly excluded from the NDVI-based analysis.

2.3.2 Modelling Scenarios and Sector-Specific Approach

To complete and fully characterize the spatiotemporal dynamics of NEE measured by EC over the February 2023 - February 2024 period at the study site, RF models were implemented according to two distinct strategies. The first strategy (Scenario 1) involved training a single global RF model using pooled data from all sectors (0–360°), representing the standard approach when sector information is not exploited; this global model served as a baseline against which the added value of the sector-specific strategy could be quantified, both in terms of point-prediction performance and reconstructed annual cumulative NEE (Sect. 3.2). In the second strategy (Scenario 2), separate RF models were trained for each landscape-based wind sector classification area and key temporal subdivision, accounting for phenological shifts such as crop harvest for instance that influence flux dynamics over the wheat and mixed-grained areas. Specifically, for each crop field, pre- and post-harvest periods were modelled independently to better capture ecosystem transitions, resulting in seven sector-specific models overall (Table 1). Both strategies used the same explanatory variables as described in Sect. 2.3.3 to ensure comparability and comparison. Because the sector-specific models were trained on markedly different numbers of observations (from 625 to 7940 per sub-period; Table 1), the sensitivity of the reconstruction to training sample size was assessed on the best-sampled sector (Sector 6, wheat; n = 12,871). Two subsets were drawn at random, without replacement, from these observations, with sizes matching those of Sector 1 (n = 6254) and Sector 3 (n = 1207), and the complete sector-specific RF pipeline (same predictors, pre-/post-harvest split and bootstrap procedure; Sect. 2.3.4) was re-run on each subset. Out-of-bag performance and annual cumulative NEE were then compared among the three training sets (Sect. 4.2, Appendix C, Fig. C1).

Table 1. Sector definition and temporal subdivision associated with the number of 10-min observations (01/02/2023 - 31/01/2024).

Sector	Land cover	Wind direction range (°)	Temporal split	Split criterion	Model ID	Number of observations	Percentage of gap-filled data
1	Hybrid (grassland/mixed grain transition)	15-70	Yes	24 May	Sector 1 - before	2981	88%
					Sector 1 - after	3273	
2	Mixed grain	70-103	Yes	24 May	Sector 2 - before	1130	94%
					Sector 2 - after	2307	
3	Ditch	103-133	No	-		1207	98%
4	Wheat	133-173	Yes	7 July	Sector 4 - before	625	95%
					Sector 4 - after	1914	
5	Wheat	173-213	Yes	7 July	Sector 5 - before	1031	95%
					Sector 5 - after	1563	

6	Wheat	213-283	Yes	7 July	Sector 6 - before Sector 6 - after	4931 7940	76%
7	Ditch	283-313	No	-		2207	96%
8	Grassland	313-15	No	-		3729	93%
4+5+6	Wheat (combined)	133-283	Yes	7 July	Sector 4+5+6 - before Sector 4+5+6 - after	6587 11417	66%

335

2.3.3 Selection variables for Random Forest modelling

We used a targeted set of explanatory variables, chosen a priori based on their established mechanistic links with NEE and their relevance in surface-atmosphere exchange studies, rather than an automated variable-selection procedure. Although methods such as Variable Selection Using Random Forest (VSURF) (Genuer et al., 2010) are commonly used to reduce
340 dimensionality prior to RF modelling, we did not apply such automated selection in the present study. All models were trained using the same set of predictors: photosynthetically active radiation (PAR), day of year (DOY), a qualitative day-night indicator, relative air humidity, soil moisture, soil temperature, wind direction, and air temperature. PAR directly regulates photosynthetic activity and light-driven variations in ecosystem CO_2 uptake; DOY captures seasonal changes in vegetation state and radiation regime. The qualitative day-night indicator distinguishes periods of daytime and nighttime activity by
345 assigning "day" to time steps with PAR > 10 μmol m^{-2} s^{-1} and "night" to those with PAR ≤ 10 μmol m^{-2} s^{-1}, and exhibit in turn contrasting drivers of respiration and assimilation; unlike the continuous PAR value, this categorical indicator lets the RF explicitly split on the day/night regime switch itself, which is useful as otherwise, tree-based models have to reconstruct that threshold indirectly from PAR at every split. Relative humidity and air temperature influence stomatal conductance and microbial respiration, while soil moisture and soil temperature jointly modulate below-ground respiration and substrate
350 availability. Wind direction was included to account for directional heterogeneity in source areas. Soil moisture and soil temperature were measured at a single location near the tower and as the other meteorological variables, were considered common to all sector-specific models; unlike NDVI, they were retained as predictors since they characterised the shared micro-meteorological and hydrological context of the site (itself part of what RF is asked to relate to the measured flux) rather than a field-specific vegetation status; we acknowledge this can represent a source of unresolved within-site variability that a
355 network of field-specific soil sensors would help to better address in future work. The importance of these variables chosen and checked for each model are provided in the Appendix B (see Sect. 2.3.4 below and Figs. B2, B3). Explicit seasonal or monthly cyclical time variables though useful in some modelling contexts (Vekuri et al., 2023), were not included here since the main temporal dynamics were already well captured by PAR, DOY and the day/night indicator, and would therefore provide largely redundant information. Moreover, the objective was to keep the model as simple and interpretable as possible,
360 especially since RF models are already able to handle non-linear temporal patterns without requiring explicit seasonal

transformations. Similarly, NDVI observations (Sect. 2.3.1) could not be directly used as predictors in the RF model, which was trained on footprint-integrated flux measurements rather than pure-field vegetation indices. At the end, this expert-driven approach ensured that all major biophysical drivers of NEE were represented while maintaining comparability across sectors and modelling exercises.

It should also be clarified how wind direction, one of the meteorological predictors, was assigned when reconstructing a continuous NEE time series for each sector. All meteorological variables come from the same single EC tower, whatever the wind direction. Each sector-specific RF model was trained and evaluated only on the time steps when the wind actually blew from within that sector's own angular range. However, to reconstruct NEE continuously for a sector, predictions were also needed for time steps when the wind blew from elsewhere, and the RF model still required a wind-direction value as input to produce a prediction. For these time steps, a wind-direction value was drawn at random from within the sector's angular range, while all other meteorological variables (PAR, air and soil temperature, humidity, etc.) were taken directly from the actual tower measurements at that time step. The sensitivity of the reconstructed fluxes to this random assignment was explicitly tested (Sect. 2.3.4, Appendix C, Fig. C2).

2.3.4 Model training, performance evaluation and uncertainty quantification

Two complementary modelling scenarios were implemented to reconstruct NEE values across the different wind sectors. In the first scenario (global model), a single Random Forest (RF) model was trained on the entire dataset, pooling observations across all wind directions (0–360°) without any sector- or period-specific stratification. In the second scenario (sector-specific models), independent RF models were trained separately for each land-cover sector, and, where relevant, for each sub-period defined by a phenological or management transition (e.g., harvest dates; Tables 1), using only the data associated with wind directions falling within the corresponding sector's angular range.

Both scenarios shared an identical RF parameterization. The number of trees was fixed at 300, consistent with previous evidence that RF performance stabilizes well below this threshold (Breiman, 2001). The number of predictors sampled at each split (mtry) followed the commonly used heuristic mtry = max(1, $\lfloor\sqrt{p}\rfloor$), where $\lfloor\cdot\rfloor$ denotes the floor function (rounding down, not to the nearest integer), where p is the number of candidate predictors (PAR, air temperature, relative humidity, wind direction, day of year, soil temperature, soil moisture content, and a day/night indicator; p = 8, yielding $\lfloor\sqrt{8}\rfloor = 2.83$, and thus mtry = 2) (Table B1).

Uncertainty was quantified identically for both scenarios too, using a bootstrap resampling procedure as providing a more robust basis for evaluating differences among vegetation types and modelling approaches, particularly during disturbance and post-harvest periods when fluxes are highly variable and non-stationary. For each retained model, B = 100 RF models were trained on independent bootstrap resamples of the corresponding training dataset (sampling with replacement, resample size equal to the original dataset size), using the same ntree and mtry values throughout. The resulting ensemble of 100 bootstrap models was used to generate, for each time step, a distribution of predicted CO_2 fluxes: the median of this distribution was

retained as the point estimate, and its 2.5th and 97.5th percentiles defined an empirical 95% prediction interval. Model performance (RMSE, MAE, R^2) was assessed using out-of-bag (OOB) predictions at the level of this outer bootstrap ensemble, rather than the internal tree-level OOB mechanism of a single RF. For each bootstrap replicate b, the subset of observations not drawn into that replicate's resample (out-of-bag for replicate b) was predicted using the RF model trained on that replicate. For each observation, the OOB predictions obtained across all replicates for which it was out-of-bag were aggregated by taking their median, yielding a single aggregated OOB prediction per observation. Metrics (RMSE, MAE and R^2) were then computed once, across the full dataset, from these aggregated OOB predictions. This OOB evaluation was applied consistently across the B = 100 bootstrap-resampled models of each scenario, providing an internal, unbiased estimate of predictive performance for both the global and sector-specific strategies, and forming the basis of the OOB validation framework used to compare the two strategies in Sect. 3.2 (Table 2). For flux reconstruction, continuous predictions were generated separately for each wind sector, using only the wind-direction range corresponding to that sector; whenever the observed wind direction fell outside this range, wind direction was randomly resampled within the sector's angular boundaries to preserve a consistent input space, while all other meteorological predictors were retained from the tower measurements. To test the sensitivity of the reconstruction to this random assignment, the complete annual reconstruction of each sector, and of the combined wheat sector (Sectors 4+5+6), was repeated five times with independent random draws of the assigned wind-direction values, all other inputs and model settings being kept identical; the annual cumulative NEE values obtained with the five draws were then compared (Sect. 4.2, Appendix C, Fig. C2). In the sector-specific scenario, each sector was predicted using its own dedicated bootstrap-ensemble model (and, where applicable, the model corresponding to the relevant sub-period). In the global-model scenario, the same bootstrap-ensemble model, trained on the pooled 0–360° dataset, was applied uniformly to generate predictions for every sector. This design allowed a direct comparison between sector-specific and global reconstructions of CO_2 fluxes, together with their associated uncertainty, across the different wind sectors.

2.4 NEE flux partitioning

NEE values reconstructed by the sector-specific RF models (Sect. 2.3.4) was partitioned into GPP and Reco for each sector and for the combined wheat sector (Sectors 4+5+6). Following Kowalski et al. (2003, 2004), daytime NEE (NEEd) can be expressed as a curvilinear (rectangular hyperbolic) function of the incident photosynthetic photon flux density (PAR):

$$NEEd = \frac{(a1.PAR)}{(a2 + PAR)} + Reco$$

where a1 is the maximum photosynthetic uptake rate at light saturation (µmol m^{-2} s^{-1}), a2 is the light level corresponding to half the maximum uptake (µmol m^{-2} s^{-1}) and Reco is the mean ecosystem respiration (µmol m^{-2} s^{-1}) at the time scale of the non-linear regression of NEEd vs PAR. Here, these three parameters were determined at daily scale for each sector-specific RF reconstruction, with GPP being negative by convention (Sect. 2.2.1). Daily Reco and GPP estimates were then summed to obtain cumulative annual Reco and GPP for each sector (Sect. 3.4, Table 3, Fig. 9).

3 Results

3.1 Site condition, measured NEE dynamics and phenology of the studied land fields

NEE followed a clear seasonal pattern with the studied site behaving predominantly as a carbon sink from February to the end of May, reflecting the progressive development of crop and grassland canopies under increasing PAR and air temperature values (Figs. 5a, b, d). A pronounced minimum in NEE (i.e. maximum net uptake) occurred around mid-May, coinciding with peak vegetative development across the three underlying land uses (wheat, grassland, mixed grain, Fig. 6). From mid-May onward, NEE values progressively shifted toward a source behaviour, associated with crop senescence and harvest events (Fig. 5c–g), before stabilising into a moderate source regime during autumn and winter. A distinct disturbance was recorded in November 2023, when an intense storm produced a sharp rainfall peak and an abrupt increase in soil moisture (Fig., 5e, f; red box), coinciding with large-amplitude, high-frequency fluctuations in the measured NEE (see Sect. 2.2.2 and Appendix A, Fig. A2). Wind direction (Fig. 5h) confirmed that the tower sampled all eight defined sectors (Table 1) over the year, although unevenly, according to the prevailing wind regime at the site (Fig. 7).

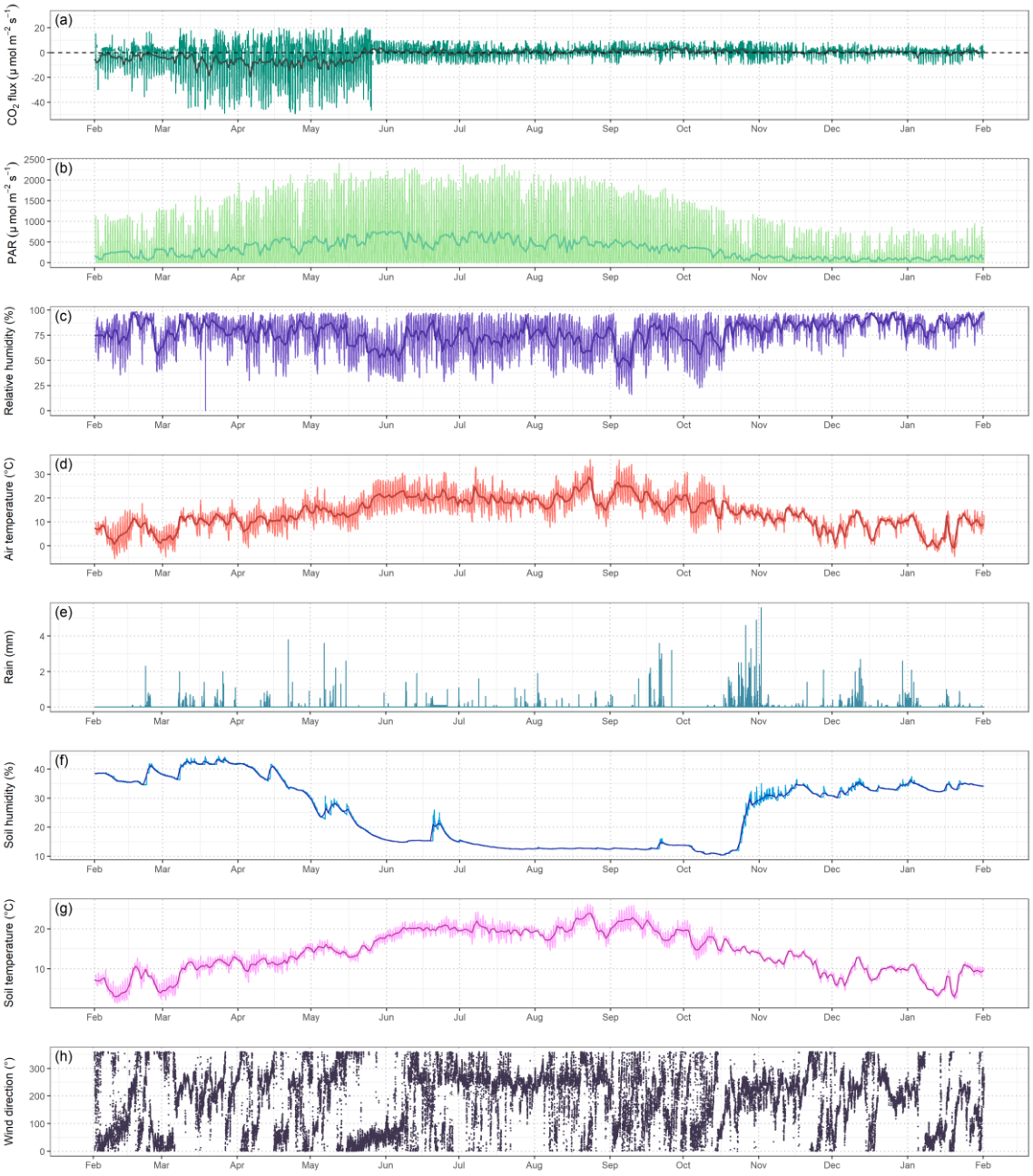


Figure 5. Eddy Covariance measured time series from 01 February 2023 to 31 January 2024 of (a.) atmospheric CO_2 flux (NEE), (b.) Photosynthetically Active Radiation (PAR), (c.) relative humidity, (d.) air temperature, (e.) rain, (f.) soil humidity, (g.) soil temperature and (h.) wind direction. For CO_2 fluxes, PAR, relative humidity, air temperature, soil humidity and soil temperature, the continuous line represents the daily average obtained from the 10 min values. CO_2 flux values correspond to filtered EC data after applying u_* and hard-limits filters as explained in Sect. 2.2.2 (see Fig. 3 too).

The MODIS NDVI time series (Fig. 6) illustrated contrasting phenological trajectories among the three underlying land uses. Both the wheat and mixed-grain fields showed a steady NDVI increase from late winter, reaching maximum canopy greenness in spring. The mixed-grain field exhibited an abrupt NDVI decline following its harvest on 24th May 2023, after which the field remained largely bare until autumn re-sowing that produced a renewed NDVI increase. The wheat field maintained high NDVI values later into the season, consistent with its later phenological cycle, and showed a comparatively smaller NDVI discontinuity at harvest because the crop was already senescent and dry at that stage. The permanent grassland field displayed the smallest seasonal amplitude, with NDVI values remaining moderate and relatively stable year-round, consistent with continuous grazing and the absence of a single, abrupt senescence event. One can notice that these independent phenological trajectories, derived from well-defined "pure" field polygons that exclude riparian vegetation (Sect. 2.3.2), provide an external, remote-sensing-based validation of the harvest dates (May, 24th and July, 7th of the year 2023) used in Sect. 2.3.2.

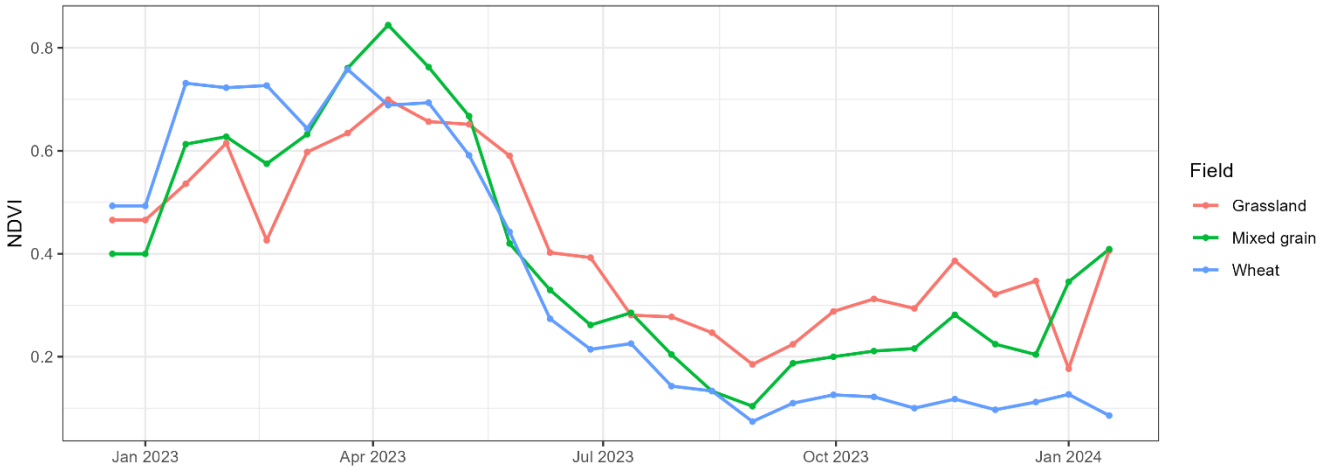


Figure 6. Temporal evolution of MODIS-derived NDVI for the three study fields from January 2023 to January 2024.

3.2 Global versus sector-specific RF modelling: point performance and annual flux reconstruction

The two modelling strategies (Scenario 1, global; Scenario 2, sector-specific) were compared using the OOB validation framework as described in Sect. 2.3.4 (n = 34,838 observations across the 13 sector × period sub-groups; Table 2). Point-prediction performance was overall very similar between the two strategies: R^2 differed by less than 0.02–0.03 and RMSE by less than 5% for most sub-groups (Table 2). Nevertheless, the global model showed a systematically narrower 95% confidence interval (IC95) than the corresponding sector-specific model in every sub-group, with a reduction of 5 to 16% depending on the sub-group, reflecting the much larger effective bootstrap training sample available for the global model (n ≈ 34,800 vs. 600–8,000 for individual sector-specific models). The sign of the point-performance difference between strategies depended on sub-group sample size: for the most heavily sampled sub-groups (n > ~3000; e.g. Sector 6-after, Sector 8, Sector 1-after), the sector-specific model matched or marginally outperformed the global model, whereas for smaller sub-groups, the global

model showed a modest advantage (e.g. R^2 + 0.06 for Sector 2-after and + 0.07 for Sector 4-after relative to the sector-specific model). R^2 varied widely among sub-groups (0.20–0.94; Table 2), but this range was driven primarily by differences in the amplitude of observed flux variability rather than by absolute model error, which remained comparatively stable across sub-groups (RMSE ≈ 1.5–2.6 µmol m^{-2} s^{-1} for the more stable post-harvest periods and ≈ 3–4.6 µmol m^{-2} s^{-1} for the higher-variability pre-harvest periods).

Table 2. Out-of-bag (OOB) performance of the sector-specific and global RF models for each of the 13 sector × period sub-groups, evaluated on the same held-out observations (n, sample size; Mean and SD, mean and standard deviation of observed flux, µmol m^{-2} s^{-1}; RMSE, root-mean-square error, µmol m^{-2} s^{-1}; IC95, width of the bootstrap 95% confidence interval, µmol m^{-2} s^{-1}).

Model ID	Observations			RMSE sector	RMSE global	R^2 sector	R^2 global	IC width sector	IC width global
	Number	Mean	Sd						
Sector 1 – before	2981	-5.12	10.75	2.98	2.97	0.92	0.92	2.71	2.53
Sector 1 – after	3273	0.97	4.7	2.05	2.09	0.81	0.81	1.66	1.55
Sector 2 – before	1130	-5.99	9.46	2.35	2.24	0.94	0.94	2.41	2.23
Sector 2 – after	2307	0.73	3.11	1.79	1.63	0.67	0.73	1.5	1.4
Sector 3	1207	-1.24	5.64	2.61	2.48	0.79	0.81	2.39	2.09
Sector 4 – before	625	-5.10	11.37	3.73	3.46	0.89	0.91	3.81	3.21
Sector 4 – after	1914	1.20	2.02	1.57	1.53	0.39	0.43	1.30	1.24
Sector 5 – before	1031	-5.14	10.79	4.63	4.56	0.82	0.82	4.12	3.64
Sector 5 – after	1563	0.95	2.18	1.95	1.96	0.20	0.20	1.63	1.42
Sector 6 – before	4931	-6.04	13.54	4.10	4.11	0.91	0.91	3.26	3.10
Sector 6 – after	7940	0.84	2.35	1.62	1.63	0.53	0.52	1.28	1.21
Sector 7	2207	-0.93	5.59	2.38	2.26	0.82	0.84	1.90	1.69
Sector 8	3729	-0.59	7.03	2.24	2.30	0.90	0.89	1.80	1.74

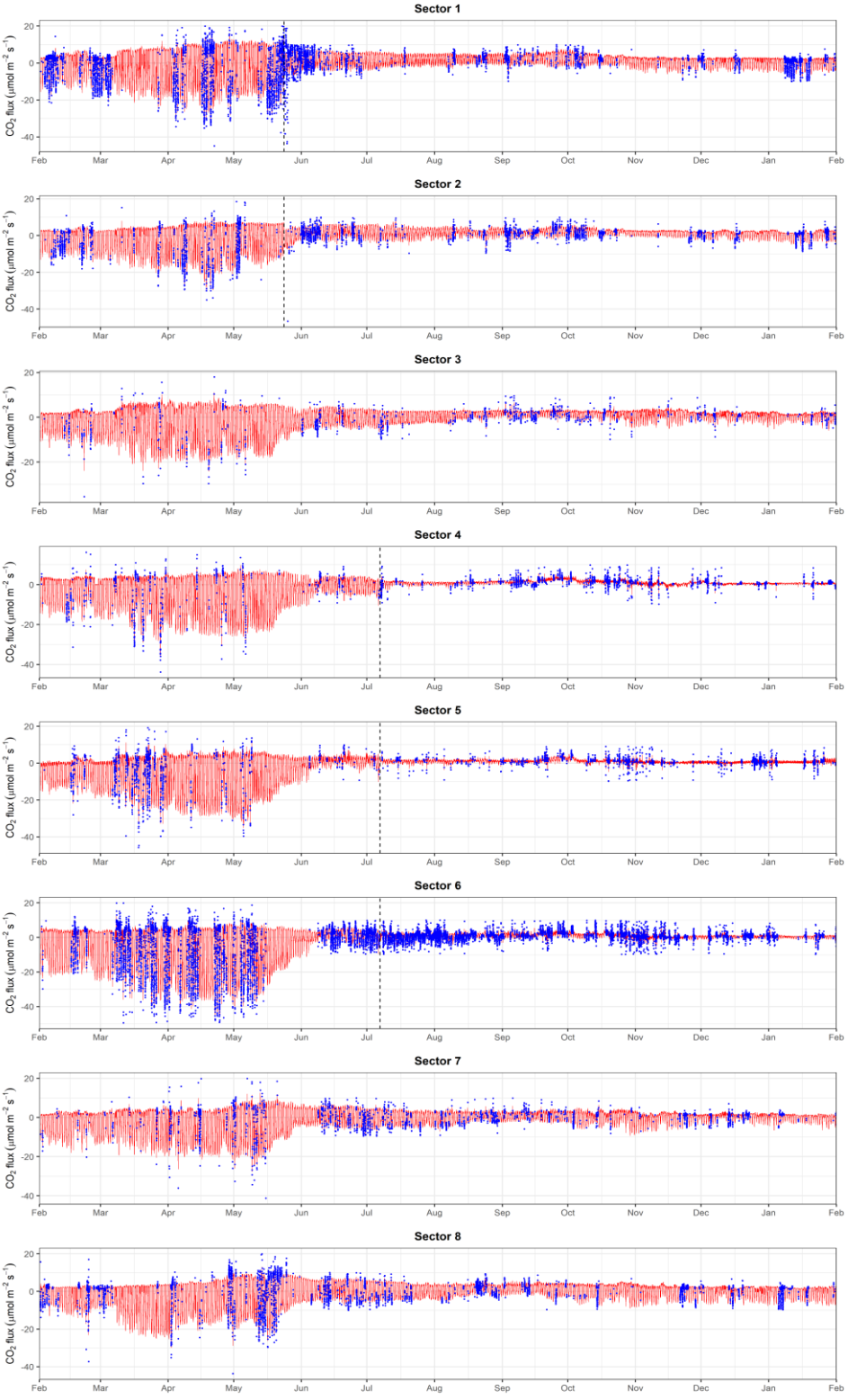

Sector 1
Sector 2
Sector 3
Sector 4
Sector 5
Sector 6
Sector 7
Sector 8
CO2 flux (μmol m-2 s-1)
20
0
-20
-40
Feb
Mar
Apr
May
Jun
Jul
Aug
Sep
Oct
Nov
Dec
Jan
Feb

Figure 7. Measured 10-min NEE values (blue dots) and sector-specific RF reconstruction (red curves; bootstrap median) for each of the eight wind sectors, from 1st February 2023 to 31st January 2024. Dashed vertical lines indicate the harvest date for the corresponding sector (24th May 2023 for Sectors 1 and 2; 7th July 2023 for Sectors 4, 5 and 6; not applicable for Sectors 3, 7 and 8).

Figure 7 shows how the 10-min NEE observations of each sector were distributed over the measurement year, together with the corresponding sector-specific reconstruction. Because a sector is sampled only when the wind blows from within its angular range, observations occurred as discrete clusters separated by gaps of a few days to several weeks, ranging from only 2% (Sector 3) to 24% (Sector 6) of the annual 10-min time steps (Table 1). Nevertheless, these clusters were well spread over the whole year in every sector, so that each sector was sampled during multiple, contrasted and widespread periods, i.e., the spring growth period, around the senescence or harvest transition, during autumn and winter seasons. Thus, the observations encompassed the two contrasting flux regimes of the annual cycle: a high-amplitude regime in spring, with daytime uptake reaching −35 to −49.4 μmol m^{-2} s^{-1}, respectively for sector 2 and 6, and a low-amplitude regime thereafter, with fluxes mostly confined within ±10 μmol m^{-2} s^{-1}. The sector-specific reconstructions reproduced this seasonal course in all eight sectors. The amplitude of the reconstructed diurnal cycle increased progressively from February to May, then collapsed at harvest in Sectors 1 and 2 (May, 24th) and during senescence (i.e., several weeks before harvest (July, 7th) in the wheat Sectors 4–6). Sector-specific features were also resolved: from late June onwards, reconstructed fluxes remained close to zero in the wheat sectors, whereas the grassland (Sector 8) maintained a distinct diurnal cycle until winter. Overall, together with the OOB statistics (Table 2), Figure 7 indicates that the observations available for each sector, despite their limited number, were sufficiently well distributed across time to cover most of the annual flux variability and to constrain all the seasonal dynamics of each sector-specific model.

This apparent equivalence between the two strategies did not hold once fluxes were reconstructed continuously over the full annual cycle for each sector (i.e. annual cumulative NEE, Fig. 8). Both strategies reproduced the same qualitative seasonal pattern (a growing sink from February to late May, a marked minimum around June, and a progressive return to source behaviour in late summer/autumn), but diverged markedly in amplitude and relative sector ranking. Under the sector-specific strategy, annual cumulative NEE values ranged from +195 gC m^{-2} (Sector 1, Hybrid) to −366 gC m^{-2} (Sector 6, Wheat), with an inter-sector range of 561 gC m^{-2}. Under the global strategy, the same sectors ranged from +164 gC m^{-2} (Sector 1) to −227 gC m^{-2} (Sector 7), a range of 391 gC m^{-2}, corresponding to an overall compression of about 30% in the amplitude of inter-sector variability (Fig. 8). This compression was uneven across sectors: comparatively small for Sector 8 (grassland, −12%) and Sector 6 (wheat, the best-sampled sector, −45%), but much stronger for Sector 4 (−71%), Sector 5 (−62%) and Sector 2 (mixed grain, −57%) (the less-sampled sub-sectors). Sector 7 (Ditch East) was a clear exception: rather than being compressed, its cumulative NEE value was amplified under the global strategy (−181 to −227 gC m^{-2}), to the point of inverting its ranking relative to Sector 6 between the two strategies. Taken together, these results show that the global and sector-specific models, despite near-equivalent OOB point performance, yield substantially different spatial pictures of the site's NEE values cumulated (extrapolated) over the full annual cycle for each sector. Because the present site combines strong sub-field

heterogeneity in land cover, phenology and management, and because the objective of this study was precisely to resolve field-scale NEE contrasts, the global model was not retained for the remainder of the analysis: all results and interpretations presented hereafter (Sects. 3.3–3.4) are then based on the sector-specific (Scenario 2) reconstructions (see Sect. 4.1 for further discussion).

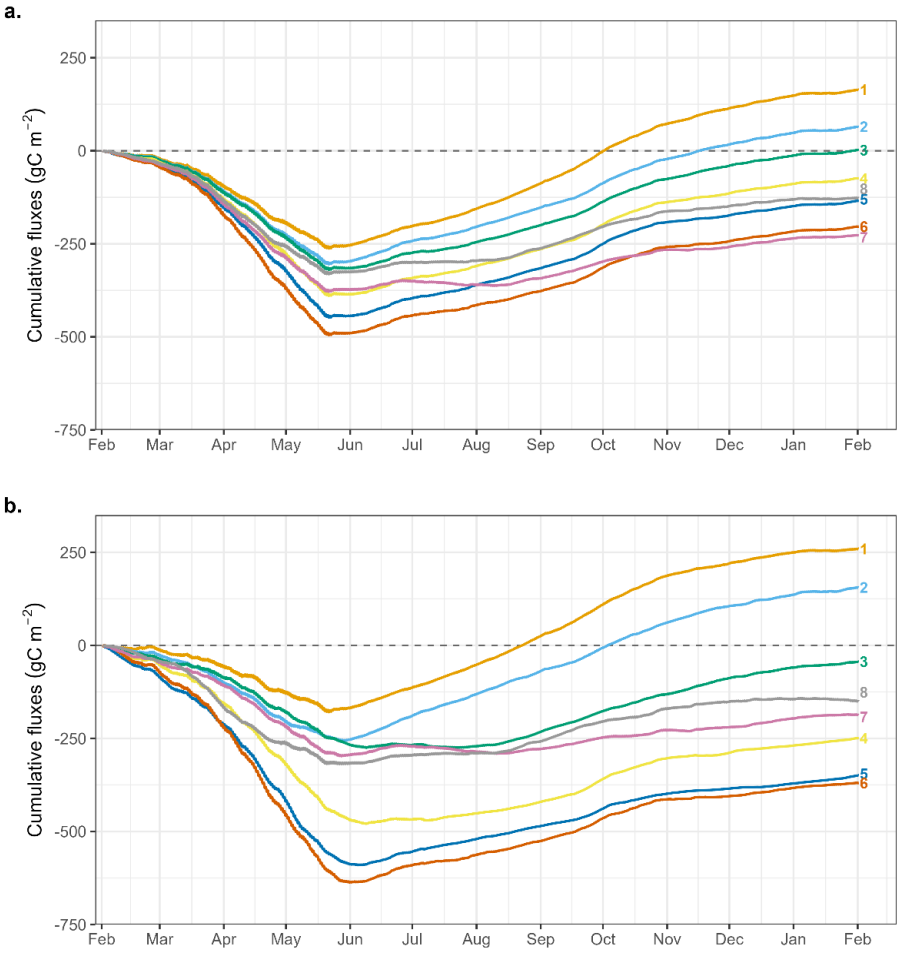


Figure 8. Annual cumulative CO_2 fluxes (cumulative NEE values) reconstructed for each of the eight sectors (Fig. 2a) with the global strategy (a, Scenario 1) and the sector-specific strategy (b., Scenario 2).

3.3 Uncertainties associated with sector-specific models and flux footprint

Uncertainty in the sector-specific reconstructions, quantified through the bootstrap 95% confidence interval (IC95) built from 100 resampled RF models (Sect. 2.3.4), varied significantly among sectors and between the pre- and post-harvest periods (Tables 1, 2, Fig. 9). Confidence intervals were systematically wider before harvest/mowing (IC95 = 2.41–4.12 µmol m^{-2} s^{-1}) than after (IC95 = 1.28–1.63 µmol m^{-2} s^{-1}), reflecting both the higher intrinsic flux variability during the active growth period

and, for several sectors, smaller pre-harvest sample sizes (i.e., n = 625 for Sector 4-before vs. n = 1914 for Sector 4-after). Among the post-harvest/stable periods, the narrowest intervals were obtained for the wheat sub-sectors 4 and 6 (IC95 = 1.28–1.30 µmol m^{-2} s^{-1}), and the widest for Sector 3 (IC95 = 2.39 µmol m^{-2} s^{-1}) and Sector 7 (IC95 = 1.90 µmol m^{-2} s^{-1}).

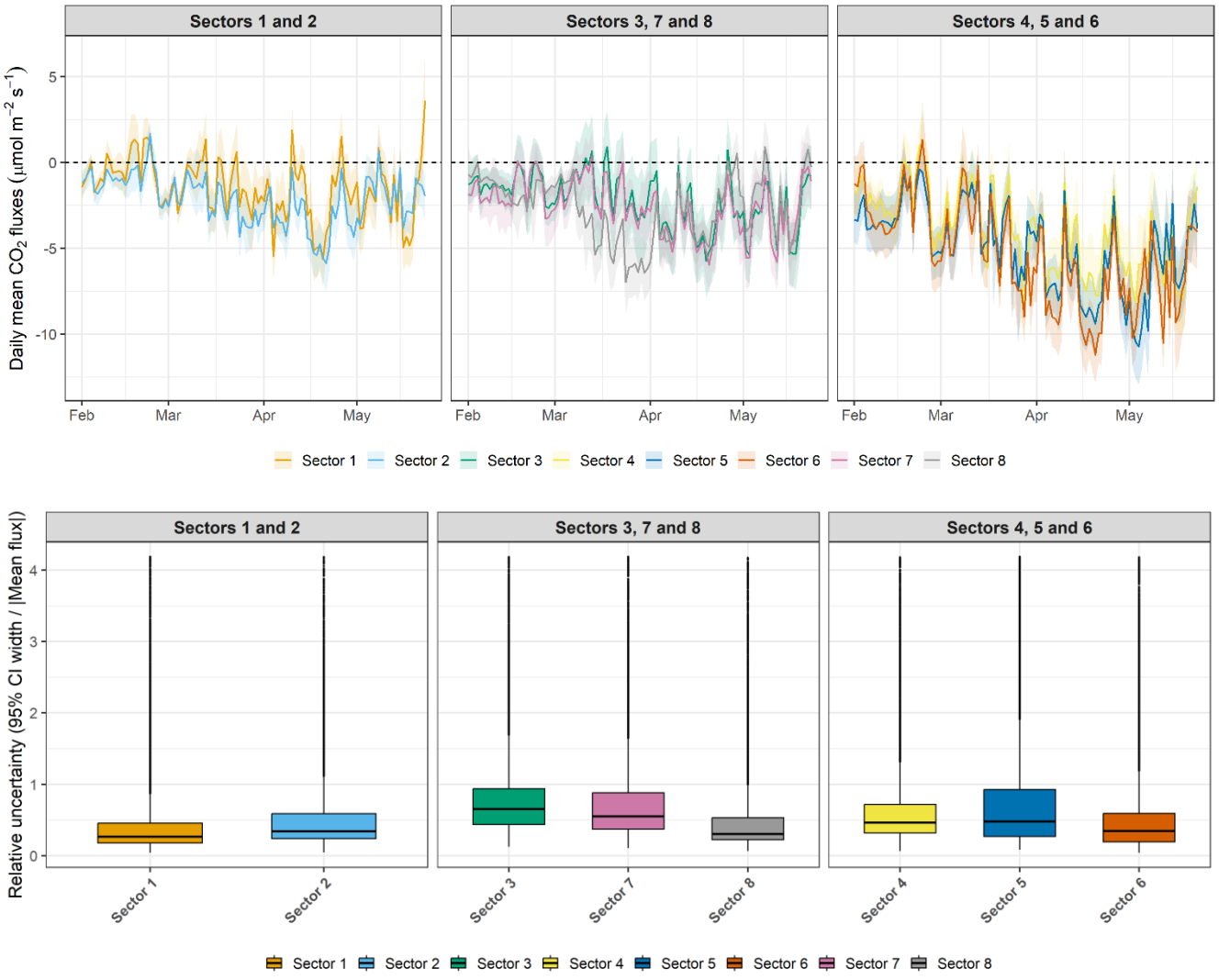


Figure 9. Reconstructed NEE dynamics and bootstrap 95% confidence intervals for each sector before harvest/mowing (1 Feb.–24 May) (above) with associated distribution of boostrap 95% confidence interval width before harvest/mowing (below).

This pattern reflects both statistical sampling effects and the spatial structure of the flux footprint relative to the position of the EC tower; the implications of this footprint geometry for the interpretation of each sector's cumulative NEE are examined in detail in the Discussion (Sect. 4.2).

3.4 NEE Partitioning into GPP and ecosystem respiration (R_{eco})

Across all sectors, annual GPP ranged from −1037 gC m⁻² (Sector 5) to −1601 gC m⁻² (Sector 8, grassland), and annual Reco from 684 gC m⁻² (Sector 5) to 1700 gC m⁻² (Sector 1) (Table 3, Fig. 10). The three wheat sub-sectors (4, 5, 6) shared a broadly similar phenological signature, i.e. moderate GPP (−1037 to −1419 gC m⁻²) combined with the lowest Reco values of the whole dataset (684 to 1050 gC m⁻²), consistent with a single, well-defined crop cycle sampled without interference from adjacent land covers. When combined, Sectors 4+5+6 (i.e. the full wheat field, 133–283°) yielded an annual NEE of −308 gC m⁻², GPP of −1298 gC m⁻² and Reco of 990 gC m⁻² (Table 3, Fig. 10); these combined values fall, as expected, within the range spanned by the three individual sub-sectors, and are closest to Sector 6 (the widest and best-sampled sub-sector, contributing the largest share of observations to the combined estimate; Table 1), while Sector 5 (the sub-sector centred on the sonic-anemometer wake) showed the most negative NEE and the lowest Reco of the three, and Sector 4 the least negative NEE. This internal consistency between the combined estimate and its three constituent sub-sectors supports the reliability of the wheat-field cumulative annual NEE as a whole (see also Sect. 3.3, 4.2).

By contrast, Sectors 1 (hybrid transition zone), 2 (mixed grain) and 8 (grassland), despite all lying within angular ranges vegetated for most of the year, displayed markedly different GPP/Reco balances (Table 3, Fig. 10). Sector 8 (grassland) combined the strongest gross uptake of all sectors (GPP = −1601 gC m⁻²) with a comparatively moderate Reco (1456 gC m⁻²), resulting in the second most negative cumulative annual NEE value of the whole site (−145 gC m⁻²) after the wheat sectors. Sector 2 (mixed grain) showed a markedly lower GPP (−1141 gC m⁻²) combined with a high Reco (1292 gC m⁻²), reflecting the loss of photosynthetic activity after the early harvest (24th May) and the subsequent bare-soil respiration; overall, Sector 2 remained a modest net source (+151 gC m⁻²). Sector 1 (hybrid) showed both a high gross uptake (GPP = −1505 gC m⁻², closer to that of the grassland than of the mixed-grain sector) and, simultaneously, the highest Reco of all eight sectors (1700 gC m⁻²), so that despite a photosynthetic capacity comparable to Sector 8, its respiratory term outweighed it and Sector 1 remained the largest net source of the whole site (+195 gC m⁻²) (Table 3, Fig. 10). This contrast between Sectors 1, 2 and 8, three sectors adjoining the grassland/mixed-grain area yet showing distinctly different NEE, GPP and Reco combinations, illustrates that superficially similar land-cover labels do not guarantee similar carbon dynamics once the underlying GPP/Reco decomposition is examined (see Sect. 4.3).

Sectors 3 and 7, both defined to isolate the two ditch/riparian corridors (Sect. 2.3.1), occupied an intermediate position relative to the other sectors: their GPP (−1147 and −1295 gC m⁻², respectively) and Reco (1115 and 1114 gC m⁻²) were both closer to the mixed-grain and hybrid values than to the wheat or grassland ones, and both sectors were net, moderate sinks (−32 and −181 gC m⁻², respectively).

Table 3. Annual cumulative estimates of NEE, GPP and Reco (gC m⁻² yr⁻¹).

	Sector 1	Sector 2	Sector 3	Sector 7	Sector 8	Sector 4	Sector 5	Sector 6	Sector 4+5+6
NEE	195	151	-32	-181	-145	-256	-353	-366	-308

GPP	-1505	-1141	-1147	-1295	-1601	-1056	-1037	-1419	-1298
Reco	1700	1292	1115	1114	1456	800	684	1050	990

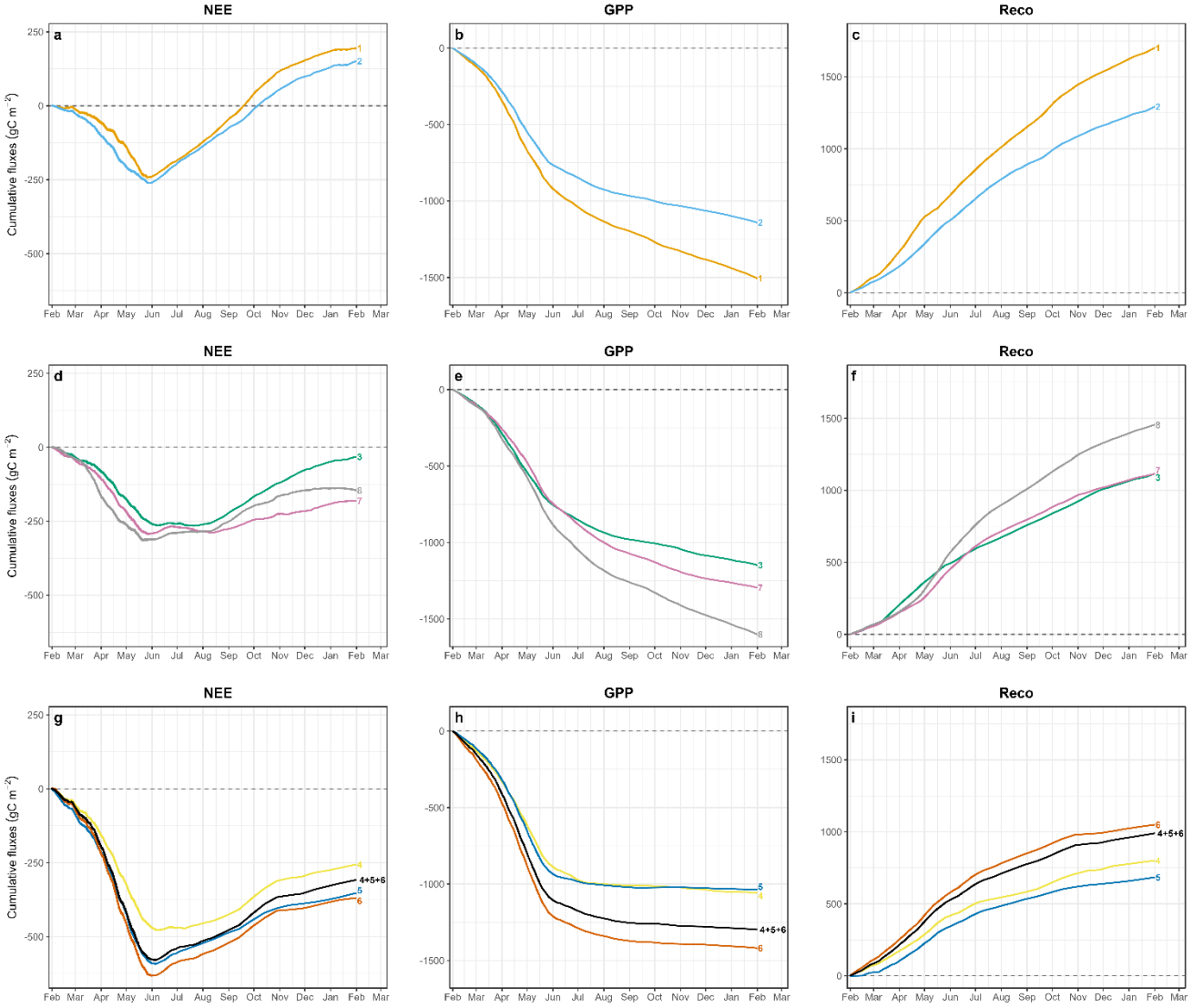


Figure 10. Cumulative estimates of NEE, GPP and Reco values for each of the eight sectors (see Table 3).

4 Discussion

4.1 Sector-specific modelling is required at a heterogeneous single-EC-tower site

The near-equivalence, and occasional slight advantage, of the global RF model in the OOB point-prediction exercise (Sect. 3.2, Table 2) reflects the classical bias-variance trade-off of ensemble tree methods (Breiman, 2001). OOB validation only tests interpolation within conditions already sampled in each sector. Here, the global model benefits from a much larger effective training sample (n ≈ 34,800 vs. 600–8,000 per sector), which narrows its bootstrap confidence intervals and lets poorly-sampled sectors "borrow" information from the pooled dataset. Although wind direction remains a global-model predictor, it competes with seven other variables at each split (mtry = $\lfloor\sqrt{8}\rfloor$ = 2) and is therefore only partially learned — consistent with the comparatively lower variable importance of wind direction in the global model relative to the sector-specific models (Appendix B, Figs. B2–B3).

This apparent equivalence breaks down once fluxes are extrapolated over the full annual cycle (Sect. 3.2, Fig. 6), a regime in which each sector must be predicted for environmental conditions it rarely experienced. Here, pooling reverses its advantage: when a sector's conditions are rare but common for the dominant sector (wheat, Sector 6), the global model's prediction shrinks toward the dominant-sector response — a shrinkage effect akin to partial pooling and Simpson's-paradox-type aggregation bias. This matches the data: the least-sampled sectors (2, 4, 5) showed the strongest compression (−59 to −70%), while the best-sampled sector showed the smallest one (−45%). Sector 3's already near-zero NEE value (−44 gC m^{-2}) fully collapsed to near zero (+2 gC m^{-2}), while Sector 7 was instead amplified — showing that shrinkage depends on covariate-space proximity to the dominant sectors, not sample size alone.

This divergence reflects the fact that day-of-year only imperfectly proxies phenological stage, so a global model that weakly resolves sector identity tends to average out physiologically distinct crop responses. This supports the conclusion that a single pooled RF model is not adequate for reconstructing field-scale annual NEE at a sub-field-heterogeneous site such as ours, even though it appears competitive - or even preferable in terms of confidence-interval width - under standard point-validation. More broadly, OOB or cross-validation metrics computed only on already-sampled conditions can substantially under-estimate the annual-NEE cost of pooling data across ecologically distinct source areas, reinforcing the case for resolving spatial heterogeneity within EC footprints (Chen et al., 2011; Oren et al., 2006; Wang et al., 2016). For this reason, the remainder of this Discussion (Sects. 4.2–4.3) focuses exclusively on the sector-specific (Scenario 2) reconstructions.

4.2 Model and experimental uncertainties: the role of the flux footprint and tower position

It is important to state explicitly what the bootstrap confidence intervals reported throughout this study (Sect. 2.3.4, 3.3) do and do not represent. These intervals quantify only the variability among the B = 100 bootstrap-resampled RF realizations for a given sector and period; they do not incorporate other, though largely discussed and addressed in the present study, sources of uncertainty that also affect the reported NEE, GPP and Reco values as deeply discussed and addressed in the present study, including measurement uncertainty in the raw EC fluxes (e.g. sensitivity to the u_* threshold, Sect. 2.2.2), uncertainty in the

attribution of individual 10-min observations to a given wind sector and uncertainty propagated through the subsequent light-response partitioning into GPP and Reco (Sect. 2.4), for which no bootstrap interval is currently reported. Two further sources of uncertainty were, however, quantified explicitly through dedicated sensitivity tests (Sects. 2.3.2 and 2.3.4; Appendix C). First, reducing the training sample of Sector 6 by about one order of magnitude (from 12,871 to 1207 observations) only moderately decreased the OOB performance (R^2 from 0.91 to 0.85; RMSE from 2.84 to 3.86 μmol m^{-2} s^{-1}), while the annual cumulative NEE changed by only 2–6% (−368, −391 and −377 gC m^{-2} for the full, medium and small training sets; Fig. C1). Second, the five random wind-direction draws yielded practically identical reconstructions in every sector: the annual cumulative NEE varied by less than 2.5 gC m^{-2} between draws (standard deviation of 0.24–1.09 gC m^{-2}), i.e. 0.4–1.2% of the annual value (2.1% for Sector 3, whose value is the closest to zero), which is more than one order of magnitude smaller than the bootstrap uncertainty envelopes and than the contrasts between sectors (Fig. C2). The absolute number of observations, and thus the gap-filled percentages reported in Table 1, is therefore not by itself a reliable indicator of how well the annual NEE is constrained, and the random wind-direction assignment does not contribute significantly to the uncertainty of the reconstructed values. The reported IC95 values should therefore be interpreted as a lower bound on the total uncertainty of the annual NEE, GPP and Reco estimates, rather than as a comprehensive uncertainty associated to annual cumulative values. Throughout this study, confidence in a given sector's estimate accordingly rests not on this statistical interval alone, but on the convergence of several complementary and largely independent lines of evidence: the spatial "cleanliness" of the flux footprint (below), the width of the bootstrap interval itself, the temporal density and phenological coverage of the underlying observations over the annual cycle (Sect. 3.2, Fig. 7) and the limited sensitivity of the reconstructed annual values to training sample size and to the wind-direction assignment (Appendix C).

Beyond the purely statistical uncertainty captured by the bootstrap confidence intervals (Sect. 3.3, Table 2, Fig. 9), the reliability of the sector-specific NEE values derived in this study is fundamentally constrained by the spatial structure of the EC flux footprint and by the fixed position of the tower relative to the surrounding land-cover mosaic (Fig. 2a). Because a single EC system was used, the "sector" attribution of each 10-min flux value is only as reliable as the assumption that the footprint for that wind direction is dominated by the target land cover; this assumption holds to very different degrees across the eight sectors defined in this study.

For the wheat field, sampled through the wide uninterrupted angular range of Sectors 4, 5 and 6 (133–283°), this assumption is comparatively well supported: no ditch, canal or riparian corridor lies within this angular range, and the footprint can reasonably be considered to sample the wheat canopy (and, secondarily, bare or senescent soil after harvest) almost exclusively. Confidence intervals for these three sub-sectors, particularly after harvest (IC95 = 1.28–1.30 μmol m^{-2} s^{-1}; Table 2), are also among the narrowest of the whole dataset. Together, these two independent lines of evidence - a spatially "clean" footprint and comparatively narrow statistical uncertainty - support together the interpretation that the reconstructed NEE, GPP and R_{eco} values for the wheat field (Sects. 3.2–3.4; Table 3) are well-constrained for this parcel relative to the other sectors of the present study; however, .the bootstrap confidence interval captures only part of the total uncertainty (see above), the sensitivity tests

further show that the wheat-field values are only marginally affected by a ten-fold reduction of the training sample and by the random wind-direction assignment (Appendix C, Figs. C1 and C2).

The situation is markedly less favourable for Sectors 1, 2, 3 and 7. Sectors 3 and 7 were explicitly defined to isolate the two ditch corridors and their riparian margins (Sect. 2.3.3); even so, given the narrow width of these features relative to the extent of the EC footprint, some contribution from the flanking crop or grassland edges cannot be excluded, and, conversely, some contribution from the ditch/riparian vegetation is very likely to persist within the crop-labelled sectors immediately adjacent to it (Sectors 1 and 2). This is consistent with the comparatively wide confidence intervals obtained for Sectors 3 and 7 (IC95 = 2.39 and 1.90 μmol m^{-2} s^{-1}, respectively; Table 2) and with the largest discrepancy found between the cumulative NEE value for Sector 1 ($\Delta \approx 64$ gC m^{-2}, $\approx 25\%$; Sect. 3.4). We therefore consider that, for the mixed-grain (Sector 2) and hybrid transition zone (Sector 1) in particular, the reconstructed yearly cumulative NEE values cannot be interpreted as unambiguous parcel-specific values in the same way as for the wheat sectors: they are best regarded as composite NEE values integrating a variable, and currently unquantified, contribution from riparian vegetation and open-ditch surfaces.

The permanent grassland (Sector 8) occupies an intermediate position. Visually and statistically, its footprint appears comparatively little affected by the adjacent ditch network, and its confidence interval (IC95 = 1.80 μmol m^{-2} s^{-1}) is only slightly wider than that of the wheat sectors, while the discrepancy between its RF-based and partitioned NEE estimates was the smallest of all eight sectors ($\Delta \approx 1$ gC m^{-2}; Sect. 3.4). While this sector's cumulative NEE value cannot be considered as unambiguously "pure" as that of the wheat field, given its position adjacent to the drainage-ditch network, the convergence of these independent lines of evidence suggests that it is comparatively reliable, and markedly less exposed to footprint contamination than the mixed-grain, hybrid or ditch sectors.

Overall, these results indicate that the practical outcome of a single-tower, wind-sector RF approach in a heterogeneous agricultural landscape does not give a uniformly annual cumulative NEE value as precise as we would like for every land cover, but rather a gradient of confidence directly related to the local footprint geometry: high confidence for spatially "isolated" covers such as the wheat field (and, to a slightly lesser extent, the grassland), and comparatively lower confidence for covers immediately adjacent to linear landscape features such as drainage ditches. Explicit footprint modelling with land-cover attribution (e.g. Kljun et al., 2015; Chen et al., 2011), applied at finer temporal resolution than the sector-averaged approach used here, or complementary plot-scale chamber measurements deployed within specific sectors, would be valuable next steps to further quantify, and potentially correct for, this residual footprint-mixing uncertainty in the mixed-grain, hybrid and ditch sectors.

4.3 Contrasting GPP and Reco balances underlying sector-level NEE

The GPP/Reco decomposition offers a more mechanistic view of why sectors bearing superficially similar land-cover labels can nonetheless display markedly different net carbon budgets (Sect. 3.4). The three wheat sub-sectors (4, 5, 6) shared a common phenological trajectory dominated by a single, well-defined annual crop cycle, so that their individual GPP and Reco values, and those of the combined Sectors 4+5+6, remained close to one another and essentially reflected the same underlying

process: a strong, synchronous photosynthetic pulse during spring growth followed by a sharp decline in both GPP and Reco after harvest (7th July). This internal consistency across spatial subdivisions of a single, homogeneous field supports treating Sectors 4+5+6 as a genuine field-scale yearly cumulative values for winter wheat.

By contrast, Sectors 1, 2 and 8 illustrate how similar apparent vegetation cover can conceal contrasting carbon dynamics. Sector 8 (grassland) combined the highest GPP of the whole site with a moderate Reco, consistent with a continuously vegetated, perennial cover subject to grazing rather than harvest, which sustains photosynthetic activity later into the season without the abrupt post-harvest respiration pulse seen in annual crops. Sector 2 (mixed grain), despite sharing an annual-crop phenology broadly similar to wheat before its early harvest (24th May), displayed a much lower GPP and a comparatively high Reco, indicating a shorter and less productive growing period combined with sustained soil respiration on bare ground for most of the year. Sector 1 (the hybrid transition zone between grassland and mixed grain, including riparian vegetation) combined a GPP close to that of the grassland (Sector 8) with the highest Reco of the whole site, i.e., behaving neither as a "pure" grassland nor as a "pure" cropland, but as a composite signal integrating perennial photosynthetic capacity with elevated, likely riparian- and ditch-driven, respiration; this explains why Sector 1, despite substantial gross uptake, is the largest net carbon source identified in this study (Sect. 3.4).

Sectors 3 and 7 (the two ditch/riparian corridors) further illustrate this gradient: their GPP and Reco values lied between those of the crop/grassland sectors and those of Sector 1, and both remained modest net sinks. Given their position directly adjoining Sectors 2 and 8 respectively (Sect. 2.3.1, 3.3), this intermediate signature is consistent with the corresponding mixture sampling of open-ditch/riparian surfaces and edge contributions from the neighbouring vegetated fields, rather than a fully homogeneous, non-vegetated ditch surface. Taken together, these results show that the wind-sector RF/partitioning approach, beyond providing annual NEE, GPP and Reco values, allows a differentiated reading of within-site phenological and management-driven contrasts that a single pooled model, or a coarser land-cover classification, would not resolve (Sect. 4.1).

4.4 Annual NEE estimates of the studied fields and implications for carbon accounting and limitations

Table 4. Annual net ecosystem exchange (NEE, in gC m^{-2} yr^{-1}) values found from this study and comparable literature. Site information and methodology are specified. Negative values indicate net CO_2 uptake (sink). See text for details of site conditions.

Reference (Location)	Vegetation/Crop	Method	Annual NEE (gC m^{-2} yr^{-1})	Notes
Jaksic et al. 2006 (Ireland)	Managed humid grassland	EC (2 years)	-193 (wet year); -258 (dry)	No moisture stress (soil > wilting point)
Senapati et al. 2014 (France)	Sown grassland (mowed)	EC (1 yr)	-476	"Mowing" management; net C storage ~+23 gC (after harvest)

Reference (Location)	Vegetation/Crop	Method	Annual NEE (gC m^{-2} yr^{-1})	Notes
Senapati et al. 2014 (France)	Sown grassland (grazed)	EC (1 yr)	-231	"Grazing" management; net C storage ~+141 gC
Wang et al., 2013 (China)	Winter wheat (crop season)	EC & auto-chamber	-251 (EC, seasonal)	Chamber EC comparison; EC flux matched AC flux within 7%
Schmidt et al. 2012 (Germany)	Winter wheat (annual)	EC (2 yrs)	-270 (Yr1); -270 (Yr2)	High uptake: field was a net source if harvest C removed
This study (France)	Permanent grassland	EC + RF model	-145	Sector 8; permanent grazed grassland; measured 2023-2024
This study (France)	Winter wheat	EC + RF model	-308	Sectors 4+5+6 combined; harvested 7 July 2023
This study (France)	Mixed grain	EC + RF model	+151	Sector 2; one-off rotation, ex-grassland; harvested 24 May 2023; footprint partly exposed to ditch

In this section and as explained before, the sector-level results are extented to the field scale targeted by this study: the wheat field is represented by Sectors 4+5+6, the permanent grassland by Sector 8 and the mixed-grain field by Sector 2, whereas Sector 1 (transition zone) and Sectors 3 and 7 (ditch corridors) are not interpreted as field budgets. Annual cumulative NEE, GPP and Reco values, derived from the Kowalski et al. (2003, 2004) partitioning (Table 3, Sect. 3.4), reveal contrasts among the four land covers of the site: the permanent grassland (Sector 8) and the winter wheat field (Sectors 4+5+6) acted as net carbon sinks (−145 and −308 gC m^{-2} yr^{-1}, respectively), whereas the mixed-grain field (Sector 2) and the hybrid transition zone (Sector 1) behaved as net carbon sources (+151 and +195 gC m^{-2} yr^{-1}). However, the confidence associated to each of these values differs markedly according to the footprint considerations as discussed in Sect. 3.3 and 4.2. Indeed, the winter wheat estimates can be considered as the most robust of the whole studied wetland (Sect. 3.3, 4.2). The combined estimate for Sectors 4+5+6 (NEE = −308 gC m^{-2} yr^{-1}) is well bracketed by its three constituent sub-sectors (NEE from −244 to −370 gC m^{-2}; Sect. 3.4) with differences mainly associated to angular width and sampling density of each sub-sector (Table 1) rather than genuine differences in the underlying crop; indeed, Sector 6, the widest and best-sampled sub-sector, dominated the combined estimate, while Sector 5 (centred on the sonic-anemometer wake, and thus more strongly affected by the u_* filtering constraints described in Sect. 2.3.1) showed the most negative NEE of the three values. This internal agreement between the combined wheat estimate and its sub-sectors, together with a footprint essentially free of ditch or riparian contamination (Sect.

3.3), supports a genuinely field-scale wheat cumulative NEE value. This sink strength is broadly consistent with other reported values for winter wheat (Table 4); for instance, Schmidt et al. (2012) found ≈ −270 gC m^{-2} yr^{-1} over two years of EC measurements, and Wang et al. (2013) reported −251 gC m^{-2} for a growing season using EC, in close agreement (within 7%) with automatic-chamber estimates. The permanent grassland (Sector 8) cumulative NEE value can be considered slightly differently: its footprint (Sect. 3.3) is comparatively little exposed to the drainage-ditch network relative to Sectors 1, 2, 3 and 7, since only the margin of the secondary ditch lies within its angular range; then its reconstructed NEE value predominantly reflected genuine grassland photosynthesis and respiration rather than a substantial mixed riparian or aquatic contribution. Its confidence interval (Table 2) is only slightly wider than that of the wheat sectors. This grassland sink strength also compares favorably with other managed, humid or grazed temperate grasslands (Table 4; Jaksic et al., 2006; Senapati et al., 2014). In any cases, the possible contribution of the adjacent ditch margin in its footprint needs to be taken into account when dealing with the quantification and associated uncertainties of this grassland field.

By contrast, NEE values derived for the mixed-grain (Sector 2, NEE = +151 gC m^{-2} yr^{-1}) and hybrid transition zone (Sector 1, NEE = +195 gC m^{-2} yr^{-1}) sectors should be interpreted with considerably more caution. Given the site configuration — both sectors lie directly adjacent to the Brune ditch and/or its secondary branch and their riparian vegetation (Sect. 2.3.1, 3.3) — the corresponding NEE, GPP and Reco values then cannot be considered fully representative of the mixed-grain crop, or of the grassland/mixed-grain transition, alone. The exceptionally high Reco recorded in Sector 1 (1700 gC m^{-2} yr^{-1}, the highest of the whole site; Sect. 4.3) most likely integrated a substantial riparian and/or ditch-adjacent respiratory signal rather than reflecting the transition vegetation alone. We therefore consider that, as constrained by a single EC tower, the mixed-grain annual NEE value given here, can't be fully quantitatively acceptable as a stand-alone, field-specific estimate, though its sign and general magnitude (i.e., net source behaviour, driven by a short and comparatively unproductive growing period followed by prolonged bare-soil respiration) can still be used to support discussion and comparisons as done in the present study. Similarly, the hybrid-zone quantitative NEE estimate should be treated with even greater caution, as a composite signal rather than a genuine parcel-specific budget (Sect. 3.3, 4.2, 4.3).

Comparing the four sectors together, the wheat and grassland cumulative NEE values both point to net carbon sinks which is broadly consistent with other reported values for comparable crop and grassland systems (Table 4) when the mixed-grain and hybrid sectors both appear as net sources of comparable, moderate magnitude. A key factor underlying and supporting our results on the contrast obtained between the wheat/grassland and mixed-grain systems is land-use history. The grassland and wheat plots have been under their respective management for many years, whereas the mixed grain was grassland before the measurement year and reverted to grassland afterward (Guignard and Pouponnot, personal communications); the mixed-grain system was thus a one-off cereal rotation rather than an established crop. Crop-rotation studies indicate that continuous annual cropping tends to reduce productivity, and thus carbon uptake, relative to long-term rotations or perennial cover, owing to changes in soil structure, nutrient cycling and microbial communities (Liebman and Dyck, 1993); biodiversity/rotation experiments have similarly shown that systems with longer-lived, diverse plant communities achieve greater and more stable productivity than single-year crops (Tilman et al., 2006). Similarly, the modest carbon uptake found for the mixed-grain sector

is consistent with its transient status: the recent conversion from grassland is probably associated with lower soil organic matter quality and microbial carbon-use efficiency, which can reduce photosynthetic capacity while still sustaining substantial post-harvest soil respiration, as reported for short-term grassland-to-cropland conversions elsewhere (Mukumbuta et al., 2019). The established winter wheat field, was almost neutral in full carbon accounting: once grain removal (≈ 250 gC m^{-2} via harvest) is considered, the sink behaviour we reported (Sects. 3.2, 3.4) would be largely offset. This agrees with other studies of long-term cereal monocultures (e.g. Schmidt et al., 2011) that find harvest removals can balance the high productivity of wheat. Finally, the hybrid sector (mixed-grain/grassland transition, riparian buffer) produced the largest net CO_2 source of the site; its amplified emissions arose from both the large respiration pulse of the mixed-grain crop after harvest and the continued respiration of the perennial grassland and riparian vegetation components integrated within its footprint (Sect. 4.3).

The present study solely focused on NEE values and harvested biomass, without incorporating all carbon pathways, in particular stocks and associated changes in soil organic carbon and lateral hydrological fluxes, which are particularly important to draw a precise integrated carbon budget of the site. Simultaneous water pCO_2 measurements conducted in November 2023 within the LRTZC project indicated mean water CO_2 emissions of 3.45 ± 4.04 µmol m^{-2} s^{-1} (data not shown) from the ditch surface, which contrast with the cumulative NEE values obtained for the surrounding fields; from previous bimonthly water carbon and discharge measurements carried out in 2017 and 2018 in the different watercourses of the Marais poitevin watershed flowing to the Aiguillon bay, an annual terrestrial carbon export from the wetland of 15 gC m^{-2} yr^{-1} was estimated (Coignot et al., 2020). These carbon fluxes (i.e. water-air CO_2 flux and carbon export values) highlight the importance of lateral aquatic fluxes that need to be taken into account to draw the whole regional carbon budget of the land-sea continuum formed by the Marais poitevin wetland and the Aiguillon tidal bay (Polsenaere, 2025) and that was out of scope for the present study.

5 Conclusions

This study shows that a single, Eddy Covariance tower, combined with wind-sector partitioning and sector-specific Random Forest modelling, can resolve contrasting annual NEE dynamics across a heterogeneous agricultural mosaic without multiple flux towers. While a pooled, sector-agnostic model matched the sector-specific models in point-prediction performance, it can strongly compress and/or invert the inter-sector contrasts once fluxes were reconstructed over the full year — a shrinkage effect toward the dominant sector's response that makes the sector-specific approach a necessary, not merely preferable, choice for such heterogeneous sites. Partitioning the fluxes into GPP and Reco confirmed these results and showed that sectors with similar land-cover labels can still have markedly different carbon dynamics. Over the study year, the permanent grassland and the winter wheat field acted as net carbon sinks (−145 and −308 gC m^{-2} yr^{-1}), while the mixed-grain field acted as net source (+151 gC m^{-2} yr^{-1}). From a quantitative and associated uncertainties point of view we particularly addressed in the present study, these estimates are not equally reliable; indeed the wheat and grassland cumulative NEE values could be considered well constrained, whereas the mixed-grain field, adjacent to drainage ditches and riparian vegetation, yielded more composite, cautiously-interpreted estimate depending on available measurements and associated wind directions too. Beyond these

limitations, this single-tower, wind-sector framework offers a transferable, low-cost alternative to multi-tower setups for resolving field-scale carbon dynamics in other heterogeneous agricultural landscapes.

Appendix A

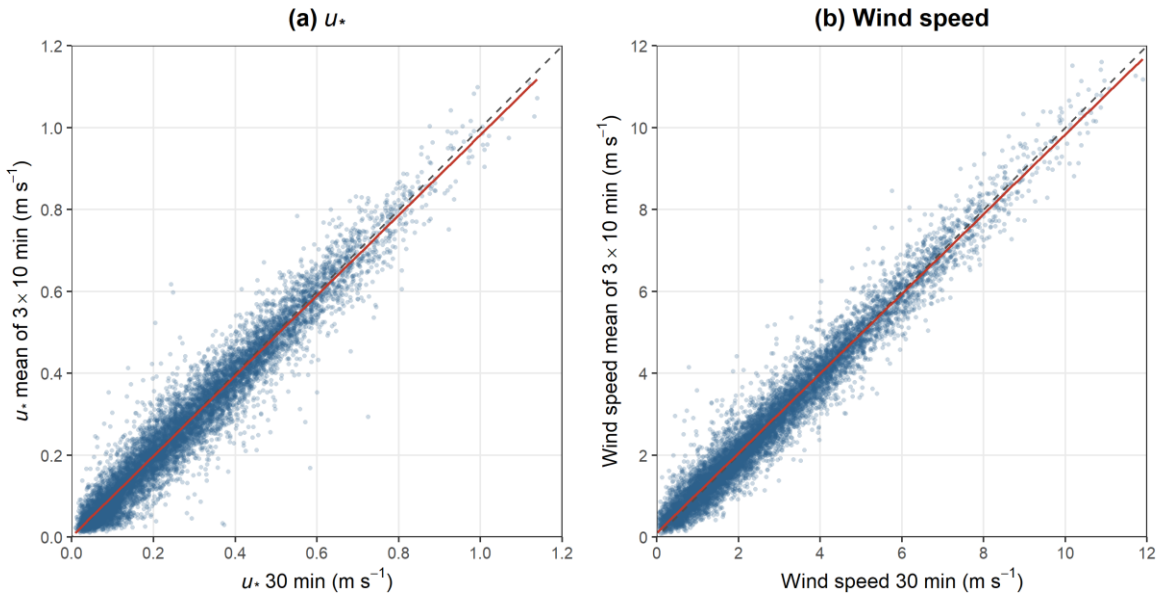


Figure A1. Friction velocity (u*) and wind speed data as the mean of the three 10 min values versus corresponding mean values obtained with an averaging time period of 30 min (Comparisons done between 10 min and 30 min data showed that, according to the land parcel, a loose between 21% (wheat, sector 213°-283° with dominant wind directions) and 49% (wheat, sector 133°-173°) of data would be obtained with a choice of 30 min mean flux calculation instead of the 10 min mean flux procedure used here)

Appendix B

Table B1. Random Forest model parametrization.

Parameter	Value description
Algorithm	Random Forest regression (RandomForest package, R)
Number of trees (ntree)	300
Number of variables tried at each split (mtry)	$\lfloor\sqrt{(\text{number of predictors})}\rfloor = \lfloor\sqrt{8}\rfloor = 2$
Node/leaf size	Default RF settings (not modified)
Predictor variables (8)	PAR, relative humidity, air temperature, wind direction, day of year (DOY), soil moisture, soil temperature, day/night category (PAR > 10)
Target variable	Filtered NEE (CO_2 flux after hard-limit/QA filtering)

Uncertainty estimation	Bootstrap aggregation, B = 100 resamples (sampling with replacement) per sector/period model
Ensemble prediction	Median of the 100 bootstrap RF predictions
95% prediction interval	2.5^{th}–97.5^{th} percentile of the 100 bootstrap predictions
Performance metrics	RMSE, MAE, R^2 (computed between observed flux and bootstrap-median prediction)

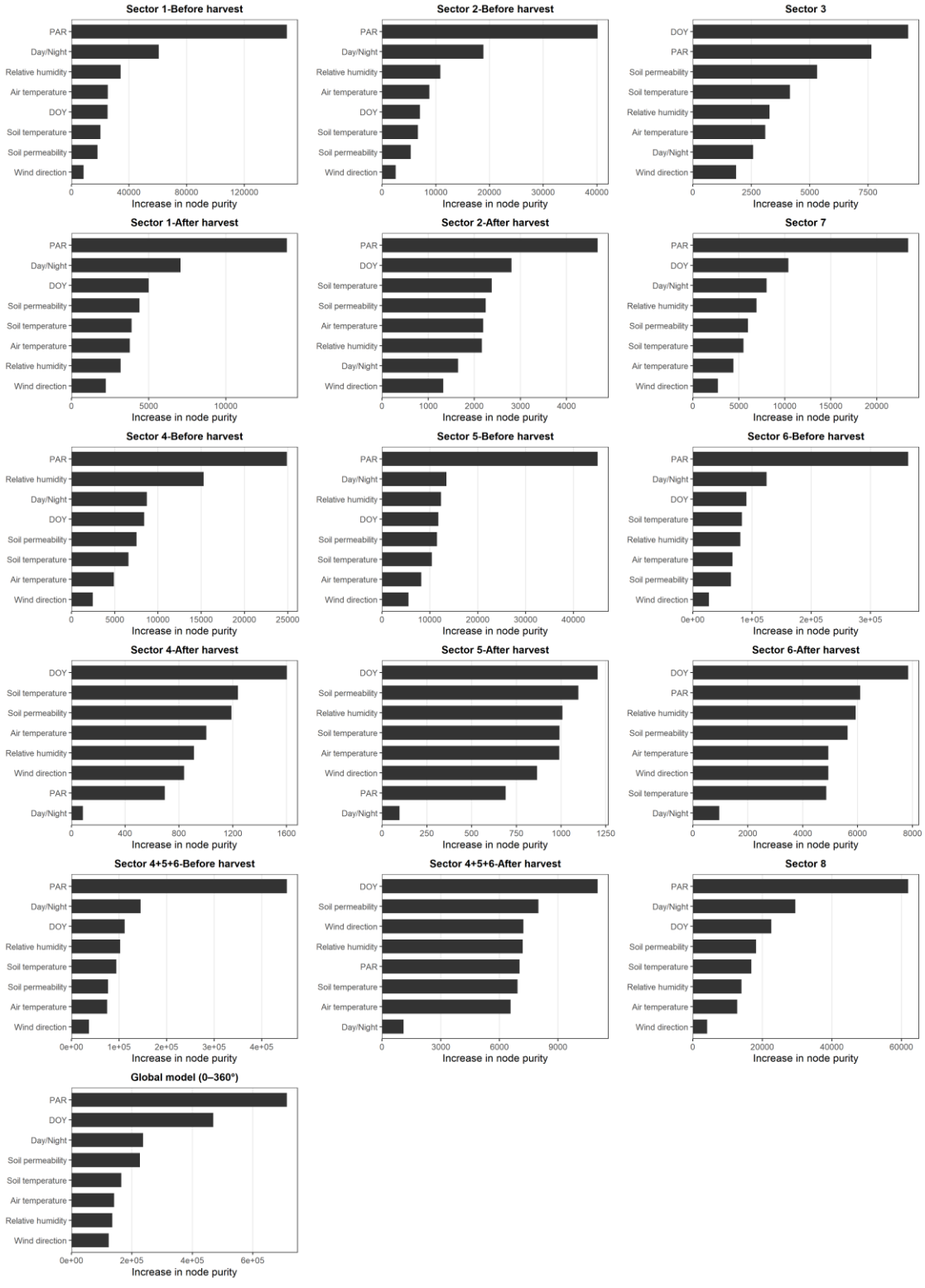

Sector 1-Before harvest
PAR
Day/Night
Relative humidity
Air temperature
DOY
Soil temperature
Soil permeability
Wind direction
0
40000
80000
120000
Increase in node purity
Sector 2-Before harvest
PAR
Day/Night
Relative humidity
Air temperature
DOY
Soil temperature
Soil permeability
Wind direction
0
10000
20000
30000
40000
Increase in node purity
Sector 3
DOY
PAR
Soil permeability
Soil temperature
Relative humidity
Air temperature
Day/Night
Wind direction
0
2500
5000
7500
Increase in node purity
Sector 1-After harvest
PAR
Day/Night
DOY
Soil permeability
Soil temperature
Air temperature
Relative humidity
Wind direction
0
5000
10000
Increase in node purity
Sector 2-After harvest
PAR
DOY
Soil temperature
Soil permeability
Air temperature
Relative humidity
Day/Night
Wind direction
0
1000
2000
3000
4000
Increase in node purity
Sector 7
PAR
DOY
Day/Night
Relative humidity
Soil permeability
Soil temperature
Air temperature
Wind direction
0
5000
10000
15000
20000
Increase in node purity
Sector 4-Before harvest
PAR
Relative humidity
Day/Night
DOY
Soil permeability
Soil temperature
Air temperature
Wind direction
0
5000
10000
15000
20000
25000
Increase in node purity
Sector 5-Before harvest
PAR
Day/Night
Relative humidity
DOY
Soil permeability
Soil temperature
Air temperature
Wind direction
0
10000
20000
30000
40000
Increase in node purity
Sector 6-Before harvest
PAR
Day/Night
DOY
Soil temperature
Relative humidity
Air temperature
Soil permeability
Wind direction
0e+00
1e+05
2e+05
3e+05
Increase in node purity
Sector 4-After harvest
DOY
Soil temperature
Soil permeability
Air temperature
Relative humidity
Wind direction
PAR
Day/Night
0
400
800
1200
1600
Increase in node purity
Sector 5-After harvest
DOY
Soil permeability
Relative humidity
Soil temperature
Air temperature
Wind direction
PAR
Day/Night
0
250
500
750
1000
1250
Increase in node purity
Sector 6-After harvest
DOY
PAR
Relative humidity
Soil permeability
Air temperature
Wind direction
Soil temperature
Day/Night
0
2000
4000
6000
8000
Increase in node purity
Sector 4+5+6-Before harvest
PAR
Day/Night
DOY
Relative humidity
Soil temperature
Soil permeability
Air temperature
Wind direction
0e+00
1e+05
2e+05
3e+05
4e+05
Increase in node purity
Sector 4+5+6-After harvest
DOY
Soil permeability
Wind direction
Relative humidity
PAR
Soil temperature
Air temperature
Day/Night
0
3000
6000
9000
Increase in node purity
Sector 8
PAR
Day/Night
DOY
Soil permeability
Soil temperature
Relative humidity
Air temperature
Wind direction
0
20000
40000
60000
Increase in node purity
Global model (0–360°)
PAR
DOY
Day/Night
Soil permeability
Soil temperature
Air temperature
Relative humidity
Wind direction
0e+00
2e+05
4e+05
6e+05
Increase in node purity

Figure B1. Variable importance of the global model (scenario 1) and across individual models (scenario 2), expressed as percentage increase in node purity.

Appendix C

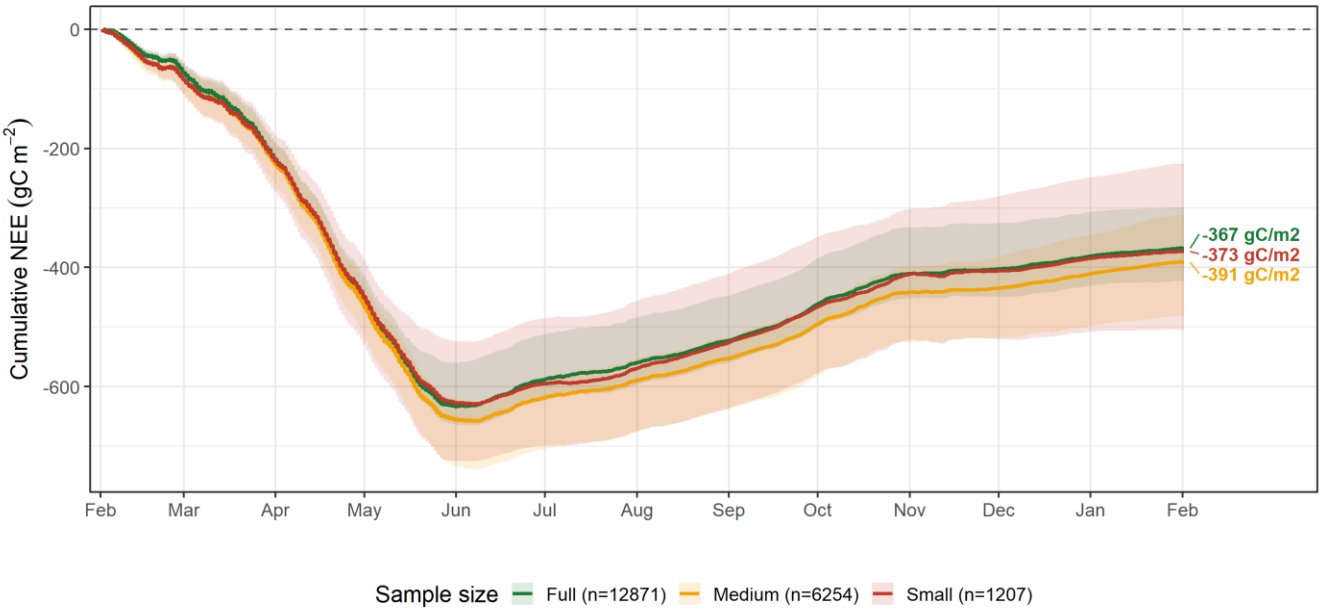


Figure C1. Sensitivity of the sector-specific reconstruction to training sample size, assessed on Sector 6 (wheat). Cumulative NEE reconstructed over the annual cycle with RF models trained on all retained observations (Full, n = 12,871) and on two random subsets (Medium, n = 6254; Small, n = 1207), using the same predictors and bootstrap procedure (B = 100). Lines are bootstrap medians and shaded areas bootstrap 95% intervals. OOB performance: R^2 = 0.91, 0.90 and 0.85, and RMSE = 2.84, 2.93 and 3.86 µmol m^{-2} s^{-1}; annual cumulative NEE = −368, −391 and −377 gC m^{-2} for the Full, Medium and Small training sets, respectively.

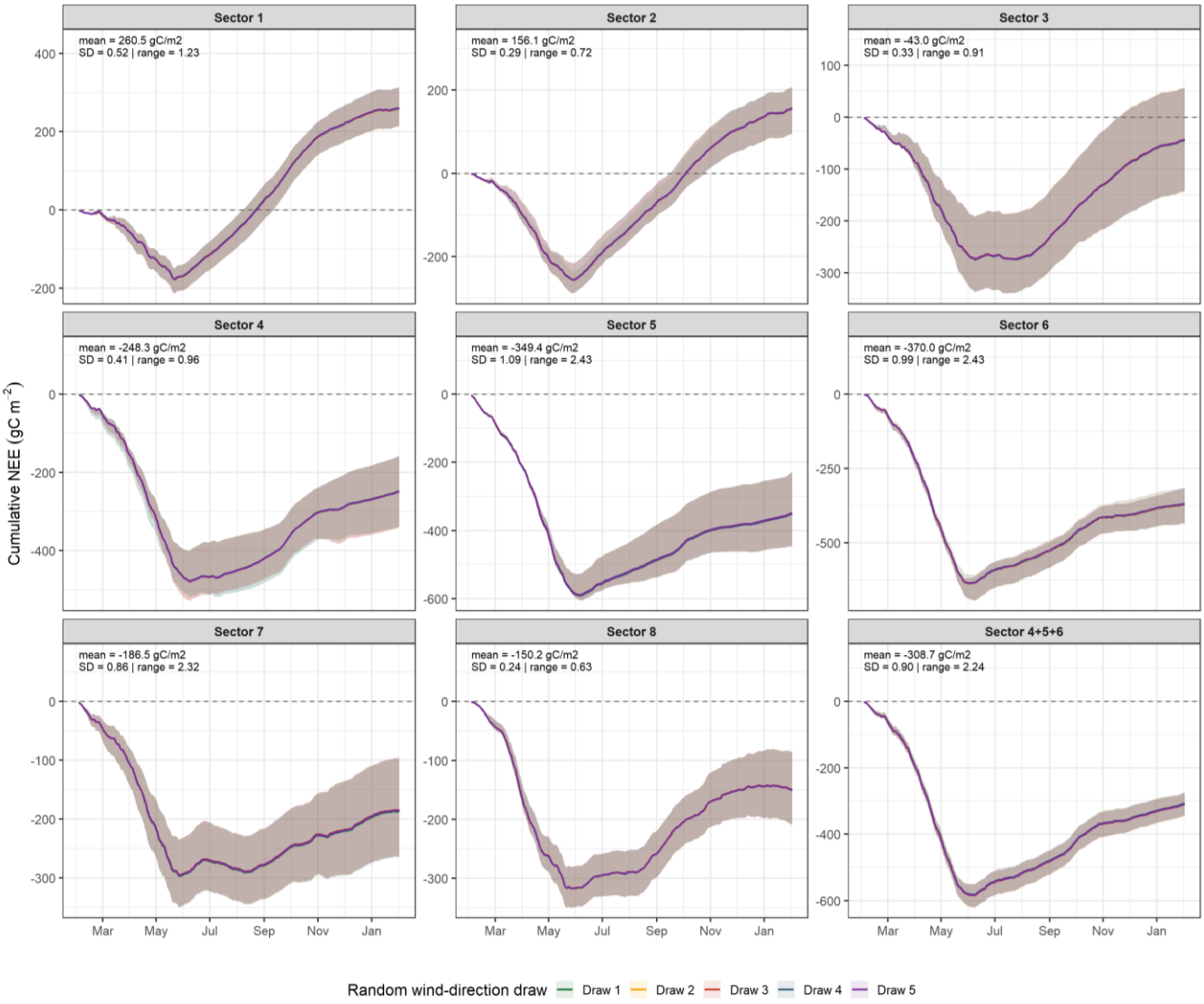


Figure C2. Sensitivity of the reconstruction to the random wind-direction assignment. Cumulative NEE reconstructed for each wind sector and for the combined wheat sector (Sectors 4+5+6) with five independent random draws of the wind-direction values assigned to off-sector time steps (coloured lines; shaded areas, bootstrap 95% intervals). The mean annual value and the standard deviation and range across the five draws (gC m^{-2}) are given in each panel.

Code/Data availability

All raw data can be provided by the corresponding authors upon request.

Author contribution

PP, EL, CP designed the study. PP, CD obtained the funding. PP, CP, JD performed the field work (EC tower deployment, maintenance, data retrieval). CP, PP, EL investigated and processed the data. PP, EL, NV, SB provided resources for data analysis. CP, PP, EL, NV, VM validated the data. CP made the graphics, wrote the draft. CP, PP, EL led the review process assisted by CD, NV, OP.

Competing interests

The authors declare that they have no conflict of interest.

Acknowledgements

This work is a contribution of Camille Pery's two years work-study contract at Ifremer (Sept. 2022-Sept. 2024) in relationships with the LRTZC project (2019-2027: *La Rochelle Territoire Zero Carbone,* PIA TIGA #25875420; Caisse des Dépôts, Région Nouvelle-Aquitaine) and related to the ANR-22-PEXF-0006 - CarboNium project. We are grateful to our Ifremer colleague Louis Costes for his help in setting up the EC station, and to Wilfried Guignard and Rodolphe Pouponnot for the culture (management) information they provided us. We thank Maxime Paschal for his work on NDVI data during his internship and Nicolas Lachaussée for organizing drone flights.

References

Agreste: Mémento de la statistique agricole – Nouvelle-Aquitaine, Ministère de l'Agriculture et de la Souveraineté alimentaire, DRAAF Nouvelle-Aquitaine, 2020.

Bajgain, R., Xiao, X., Basara, J., Wagle, P., Zhou, Y., Mahan, H., Gowda, P., McCarthy, H. R., Northup, B., Neel, J., and Steiner, J.: Carbon dioxide and water vapor fluxes in winter wheat and tallgrass prairie in central Oklahoma, Sci. Total Environ., 644, 1511–1524, https://doi.org/10.1016/j.scitotenv.2018.07.010, 2018.

Baldocchi, D. D.: How eddy covariance flux measurements have contributed to our understanding of Global Change Biology, Glob. Change Biol., 26, 242–260, https://doi.org/10.1111/gcb.14807, 2020.

Barr, A. G., Richardson, A. D., Hollinger, D. Y., Papale, D., Arain, M. A., Black, T. A., Bohrer, G., Dragoni, D., Fischer, M. L., Gu, L., Law, B. E., Margolis, H. A., McCaughey, J. H., Munger, J. W., Oechel, W., and Schaeffer, K.: Use of change-point detection for friction–velocity threshold evaluation in eddy-covariance studies, Agric. For. Meteorol., 171–172, 31–45, https://doi.org/10.1016/j.agrformet.2012.11.023, 2013.

Bolsée, S., Dupont, S., Lamaud, E., Irvine, M., Lafont, S., Chipeaux, C., Garrigou, C., Bonnefond, J.M., Domec, J.C., Loustau, D. : Wind flow dynamics over a photovoltaic power plant: comparison with a vegetated canopy, in preparation, 2026

Bou-Zeid, E., Anderson, W., Katul, G. G., and Mahrt, L.: The Persistent Challenge of Surface Heterogeneity in Boundary-Layer Meteorology: A Review, Bound.-Layer Meteorol., 177, 227–245, https://doi.org/10.1007/s10546-020-00551-8, 2020.

Breiman, L.: Random Forests, Mach. Learn., 45, 5–32, https://doi.org/10.1023/A:1010933404324, 2001.

Burba, G.: Eddy Covariance Method for Scientific, Industrial, Agricultural and Regulatory Applications: A Field Book on Measuring Ecosystem Gas Exchange and Areal Emission Rates, https://doi.org/10.13140/RG.2.1.4247.8561, 2013.

Butzer, K. W.: French Wetland Agriculture in Atlantic Canada and Its European Roots: Different Avenues to Historical Diffusion, Ann. Assoc. Am. Geogr., 92, 451–470, https://doi.org/10.1111/1467-8306.00299, 2002.Chen, B., Coops, N. C., Fu, D., Margolis, H. A., Amiro, B. D., Barr, A. G., Black, T. A., Arain, M. A., Bourque, C. P.-A., Flanagan, L. B., Lafleur, P. M., McCaughey, J. H., and Wofsy, S. C.: Assessing eddy-covariance flux tower location bias across the Fluxnet-Canada research network based on remote sensing and footprint modelling, Agric. For. Meteorol., 151, 87–100, https://doi.org/10.1016/j.agrformet.2010.09.005, 2011.

Chu, H., Baldocchi, D. D., Poindexter, C., Abraha, M., Desai, A. R., Bohrer, G., Arain, M. A., Griffis, T., Blanken, P. D., O'Halloran, T. L., Thomas, R. Q., Zhang, Q., Burns, S. P., Frank, J. M., Christian, D., Brown, S., Black, T. A., Gough, C. M., Law, B. E., Lee, X., Chen, J., Reed, D. E., Massman, W. J., Clark, K., Hatfield, J., Prueger, J., Bracho, R., Baker, J. M., and Martin, T. A.: Temporal dynamics of aerodynamic canopy height derived from eddy covariance momentum flux data across North American flux networks, Geophys. Res. Lett., 45, 9275–9287, https://doi.org/10.1029/2018GL079306, 2018.

Coignot, E., Polsenaere, P., Soletchnik, P., Le Moine, O., Souchu, P., Joyeux, E., Le Roy, Y., Guéret, J.-P., Froud, L., Gallais, R., Chourré, E., Chaigneau, L., Soletchnik, P., Le Moine, O., Souchu, P., Joyeux, E., Le Roy, Y., Guéret, J.-P., Froud, L., Gallais, R., Chourré, E., and Chaigneau, L.: Variabilité spatio-temporelle des nutriments et du carbone et flux associés le long d'un continuum terrestre-aquatique tempéré (Marais poitevin – Baie de l'Aiguillon – Pertuis Breton), 2020.

Didan, K.: MODIS/Terra Vegetation Indices 16-Day L3 Global 250m SIN Grid V061, NASA EOSDIS Land Processes Distributed Active Archive Center [data set], https://doi.org/10.5067/MODIS/MOD13Q1.061, 2021.

Friedlingstein, P., O'Sullivan, M., Jones, M. W., Andrew, R. M., Hauck, J., Landschützer, P., Le Quéré, C., Li, H., Luijkx, I. T., Olsen, A., Peters, G. P., Peters, W., Pongratz, J., Schwingshackl, C., Sitch, S., Canadell, J. G., Ciais, P., Jackson, R. B., Alin, S. R., Arneth, A., Arora, V., Bates, N. R., Becker, M., Bellouin, N., Berghoff, C. F., Bittig, H. C., Bopp, L., Cadule, P., Campbell, K., Chamberlain, M. A., Chandra, N., Chevallier, F., Chini, L. P., Colligan, T., Decayeux, J., Djeutchouang, L. M., Dou, X., Duran Rojas, C., Enyo, K., Evans, W., Fay, A. R., Feely, R. A., Ford, D. J., Foster, A., Gasser, T., Gehlen, M., Gkritzalis, T., Grassi, G., Gregor, L., Gruber, N., Gürses, Ö., Harris, I., Hefner, M., Heinke, J., Hurtt, G. C., Iida, Y., Ilyina, T., Jacobson, A. R., Jain, A. K., Jarníková, T., Jersild, A., Jiang, F., Jin, Z., Kato, E., Keeling, R. F., Klein Goldewijk, K., Knauer, J., Korsbakken, J. I., Lan, X., Lauvset, S. K., Lefèvre, N., Liu, Z., Liu, J., Ma, L., Maksyutov, S., Marland, G., Mayot, N., McGuire, P. C., Metzl, N., Monacci, N. M., Morgan, E. J., Nakaoka, S.-I., Neill, C., Niwa, Y., Nützel, T., Olivier, L., Ono, T., Palmer, P. I., Pierrot, D., Qin, Z., Resplandy, L., Roobaert, A., Rosan, T. M., Rödenbeck, C., Schwinger, J., Smallman, T. L., Smith, S. M., Sospedra-Alfonso, R., Steinhoff, T., et al.: Global Carbon Budget 2024, Earth Syst. Sci. Data, 17, 965–1039, https://doi.org/10.5194/essd-17-965-2025, 2025.

Gao, D., Yao, J., Yu, S., Ma, Y., Li, L., and Gao, Z.: Eddy Covariance CO2 Flux Gap Filling for Long Data Gaps: A Novel Framework Based on Machine Learning and Time Series Decomposition, Remote Sens., 15, 2695, https://doi.org/10.3390/rs15102695, 2023.

Gash, J. H. C. and Culf, A. D.: Applying a linear detrend to eddy correlation data in realtime, Bound.-Layer Meteorol., 79, 301–306, https://doi.org/10.1007/BF00119443, 1996.

Genuer, R., Poggi, J.-M., and Tuleau-Malot, C.: Variable selection using random forests, Pattern Recognit. Lett., 31, 2225–2236, https://doi.org/10.1016/j.patrec.2010.03.014, 2010.

Gu, L., Falge, E. M., Boden, T., Baldocchi, D. D., Black, T. A., Saleska, S. R., Suni, T., Verma, S. B., Vesala, T., Wofsy, S. C., and Xu, L.: Objective threshold determination for nighttime eddy flux filtering, Agric. For. Meteorol., 128, 179–197, https://doi.org/10.1016/j.agrformet.2004.11.006, 2005.

Jaksic, V., Kiely, G., Albertson, J., Oren, R., Katul, G., Leahy, P., and Byrne, K. A.: Net ecosystem exchange of grassland in contrasting wet and dry years, Agric. For. Meteorol., 139, 323–334, https://doi.org/10.1016/j.agrformet.2006.07.009, 2006.

Kirschbaum, M. U. F.: The temperature dependence of soil organic matter decomposition, and the effect of global warming on soil organic C storage, Soil Biol. Biochem., 27, 753–760, https://doi.org/10.1016/0038-0717(94)00242-S, 1995.

Kljun, N., Calanca, P., Rotach, M. W., and Schmid, H. P.: A simple parameterisation for flux footprint predictions, Bound.-Layer Meteorol., 112, 503–523, https://doi.org/10.1023/B:BOUN.0000030653.71031.96, 2004.

Kljun, N., Calanca, P., Rotach, M. W., and Schmid, H. P.: A simple two-dimensional parameterisation for Flux Footprint Prediction (FFP), Geosci. Model Dev., 8, 3695–3713, https://doi.org/10.5194/gmd-8-3695-2015, 2015.

Knauer, J., Zaehle, S., Medlyn, B. E., Reichstein, M., Williams, C. A., Migliavacca, M., De Kauwe, M. G., Werner, C., Keitel, C., Kolari, P., Limousin, J.-M., and Linderson, M.-L.: Towards physiologically meaningful water-use efficiency estimates from eddy covariance data, Glob. Change Biol., 24, 694–710, https://doi.org/10.1111/gcb.13893, 2018.

Kormann, R. and Meixner, F. X.: An analytical footprint model for non-neutral stratification, Bound.-Layer Meteorol., 99, 207–224, https://doi.org/10.1023/A:1018991015119, 2001.

Kowalski, S., Sartore, M., Burlett, R., Berbigier, P., and Loustau, D.: The annual carbon budget of a French pine forest (Pinus pinaster) following harvest, Glob. Change Biol., 9, 1051–1065, https://doi.org/10.1046/j.1365-2486.2003.00627.x, 2003.

Kowalski, A. S., Loustau, D., Berbigier, P., Manca, G., Tedeschi, V., Borghetti, M., Valentini, R., Kolari, P., Berninger, F., Rannik, Ü., Hari, P., Rayment, M., Mencuccini, M., Moncrieff, J., and Grace, J.: Paired comparison of carbon exchange between undisturbed and regenerating stands in four managed forests in Europe, Glob. Change Biol., 10, 1707–1723, https://doi.org/10.1111/j.1365-2486.2004.00846.x, 2004.

Kumari, S., Kambhammettu, B. V. N. P., and Niyogi, D.: Sensitivity of Analytical Flux Footprint Models in Diverse Source-Receptor Configurations: A Field Experimental Study, J. Geophys. Res. Biogeosciences, 125, e2020JG005694, https://doi.org/10.1029/2020JG005694, 2020.

Liebman, M. and Dyck, E.: Crop Rotation and Intercropping Strategies for Weed Management, Ecol. Appl., 3, 92–122, https://doi.org/10.2307/1941795, 1993.

Liu, L., Zhou, W., Guan, K., Peng, B., Xu, S., Tang, J., Zhu, Q., Till, J., Jia, X., Jiang, C., Wang, S., Qin, Z., Kong, H., Grant, R., Mezbahuddin, S., Kumar, V., and Jin, Z.: Knowledge-guided machine learning can improve carbon cycle quantification in agroecosystems, Nat. Commun., 15, 357, https://doi.org/10.1038/s41467-023-43860-5, 2024.

Lloyd, J. and Taylor, J. A.: On the Temperature Dependence of Soil Respiration, Funct. Ecol., 8, 315–323, https://doi.org/10.2307/2389824, 1994.

Mahecha, M. D., Reichstein, M., Carvalhais, N., Lasslop, G., Lange, H., Seneviratne, S. I., Vargas, R., Ammann, C., Arain, M. A., Cescatti, A., Janssens, I. A., Migliavacca, M., Montagnani, L., and Richardson, A. D.: Global Convergence in the Temperature Sensitivity of Respiration at Ecosystem Level, Science, 329, 838–840, https://doi.org/10.1126/science.1189587, 2010.

Mayen, J., Polsenaere, P., Lamaud, É., Arnaud, M., Kostyrka, P., Bonnefond, J.-M., Geairon, P., Gernigon, J., Chassagne, R., Lacoue-Labarthe, T., Regaudie de Gioux, A., and Souchu, P.: Atmospheric CO_2 exchanges measured by eddy covariance over a temperate salt marsh and influence of environmental controlling factors, Biogeosciences, 21, 993–1016, https://doi.org/10.5194/bg-21-993-2024, 2024.

Mayen, J., Polsenaere, P., Regaudie de Gioux, A., Deborde, J., Collin, K., Le Merrer, Y., Foucault, É., Ouisse, V., André, L., Arnaud, M., Kostyrka, P., Lamaud, É., Abril, G., and Souchu, P.: Aquatic metabolism influences temporal variations of water carbon and atmospheric carbon dioxide fluxes in a temperate salt marsh, Biogeosciences, 22, 5387–5411, https://doi.org/10.5194/bg-22-5387-2025, 2025.

Moreaux, V., Longdoz, B., Berveiller, D., Delpierre, N., Dufrêne, E., Bonnefond, J.-M., Chipeaux, C., Joffre, R., Limousin, J.-M., Ourcival, J.-M., Klumpp, K., Darsonville, O., Brut, A., Tallec, T., Ceschia, E., Panthou, G., and Loustau, D.: Environmental control of land-atmosphere CO2 fluxes from temperate ecosystems: a statistical approach based on homogenized time series from five land-use types, Tellus B Chem. Phys. Meteorol., 72, 2020.

Mukumbuta, I., Shimizu, M., and Hatano, R.: Short-term land-use change from grassland to cornfield increases soil organic carbon and reduces total soil respiration, Soil Tillage Res., 186, 1–10, 2019.

Novick, K. A., Ficklin, D. L., Stoy, P. C., Williams, C. A., Bohrer, G., Oishi, A. C., Papuga, S. A., Blanken, P. D., Noormets, A., Sulman, B. N., Scott, R. L., Wang, L., and Phillips, R. P.: The increasing importance of atmospheric demand for ecosystem water and carbon fluxes, Nat. Clim. Change, 6, 1023–1027, https://doi.org/10.1038/nclimate3114, 2016.

Oren, R., Hsieh, C.-I., Stoy, P., Albertson, J., McCarthy, H. R., Harrell, P., and Katul, G. G.: Estimating the uncertainty in annual net ecosystem carbon exchange: spatial variation in turbulent fluxes and sampling errors in eddy-covariance measurements, Glob. Change Biol., 12, 883–896, https://doi.org/10.1111/j.1365-2486.2006.01131.x, 2006.

Papale, D., Reichstein, M., Aubinet, M., Canfora, E., Bernhofer, C., Kutsch, W., Longdoz, B., Rambal, S., Valentini, R., Vesala, T., and Yakir, D.: Towards a standardized processing of Net Ecosystem Exchange measured with eddy covariance technique: algorithms and uncertainty estimation, Biogeosciences, 3, 571–583, https://doi.org/10.5194/bg-3-571-2006, 2006.

Polsenaere, P., Lamaud, E., Lafon, V., Bonnefond, J.-M., Bretel, P., Delille, B., Deborde, J., Loustau, D. and Abril, G.: Spatial and temporal CO2 exchanges measured by Eddy Covariance over a temperate intertidal flat and their relationships to net ecosystem production, Biogeosciences, 9, 249–268, https://doi.org/10.5194/bg-9-249-2012, 2012.

Polsenaere, P.: Dynamique du carbone en zone côtière tempérée: processus biogéochimiques et échanges aux interfaces terre – zone côtière – atmosphère. HDR. https://archimer.ifremer.fr/doc/00993/110419/, 2025.

Reichstein, M., Ciais, P., Papale, D., Valentini, R., Running, S., Viovy, N., Cramer, W., Granier, A., Ogée, J., Allard, V., Aubinet, M., Bernhofer, Chr., Buchmann, N., Carrara, A., Grünwald, T., Heimann, M., Heinesch, B., Knohl, A., Kutsch, W., Loustau, D., Manca, G., Matteucci, G., Miglietta, F., Ourcival, J. m., Pilegaard, K., Pumpanen, J., Rambal, S., Schaphoff, S., Seufert, G., Soussana, J.-F., Sanz, M.-J., Vesala, T., and Zhao, M.: Reduction of ecosystem productivity and respiration during the European summer 2003 climate anomaly: a joint flux tower, remote sensing and modelling analysis, Glob. Change Biol., 13, 634–651, https://doi.org/10.1111/j.1365-2486.2006.01224.x, 2007.

Reynolds: I. On the theory of lubrication and its application to Mr. Beauchamp tower's experiments, including an experimental determination of the viscosity of olive oil, Proc. R. Soc. Lond., 40, 191–203, https://doi.org/10.1098/rspl.1886.0021, 1886.

Schmidt, M., Reichenau, T. G., Fiener, P., and Schneider, K.: The carbon budget of a winter wheat field: An eddy covariance analysis of seasonal and inter-annual variability, Agric. For. Meteorol., 165, 114–126, https://doi.org/10.1016/j.agrformet.2012.05.012, 2012.

Schmidt, M. W. I., Torn, M. S., Abiven, S., Dittmar, T., Guggenberger, G., Janssens, I. A., Kleber, M., Kögel-Knabner, I., Lehmann, J., Manning, D. A. C., Nannipieri, P., Rasse, D. P., Weiner, S., and Trumbore, S. E.: Persistence of soil organic matter as an ecosystem property, Nature, 478, 49–56, https://doi.org/10.1038/nature10386, 2011.

Senapati, N., Chabbi, A., Gastal, F., Smith, P., Mascher, N., Loubet, B., Cellier, P., and Naisse, C.: Net carbon storage measured in a mowed and grazed temperate sown grassland shows potential for carbon sequestration under grazed system, Carbon Manag., 5, 131, https://doi.org/10.1080/17583004.2014.912863, 2014.

Tilman, D., Reich, P. B., and Knops, J. M. H.: Biodiversity and ecosystem stability in a decade-long grassland experiment, Nature, 441, 629–632, https://doi.org/10.1038/nature04742, 2006.

Vekuri, H., Tuovinen, J.-P., Kulmala, L., Papale, D., Kolari, P., Aurela, M., Laurila, T., Liski, J., and Lohila, A.: A Widely Used Eddy Covariance Gap-Filling Method Creates Systematic Bias in Carbon Balance Estimates, Scientific Reports, 13, 1720, https://doi.org/10.1038/s41598-023-28827-2, 2023.

Vickers, D. and Mahrt, L.: Quality Control and Flux Sampling Problems for Tower and Aircraft Data, 1997.

Wang, H., Jia, G., Zhang, A., and Miao, C.: Assessment of spatial representativeness of eddy covariance flux data from flux tower to regional grid, Remote Sens., 8, 742, https://doi.org/10.3390/rs8090742, 2016.

Wang, K., Liu, C., Zheng, X., Pihlatie, M., Li, B., Haapanala, S., Vesala, T., Liu, H., Wang, Y., Liu, G., and Hu, F.: Comparison between eddy covariance and automatic chamber techniques for measuring net ecosystem exchange of carbon dioxide in cotton and wheat fields, Biogeosciences, 10, 6865–6877, https://doi.org/10.5194/bg-10-6865-2013, 2013.

Wohlfahrt, G. and Gu, L.: The many meanings of gross photosynthesis and their implication for photosynthesis research from leaf to globe, Plant Cell Environ., 38, 2500–2507, https://doi.org/10.1111/pce.12569, 2015.

Wu, L., Miao, H., and Liu, T.: Development in Agricultural Ecosystems' Carbon Emissions Research: A Visual Analysis Using CiteSpace, Agronomy, 14, 1288, https://doi.org/10.3390/agronomy14061288, 2024.

Zeng, J., Matsunaga, T., Tan, Z.-H., Saigusa, N., Shirai, T., Tang, Y., Peng, S., and Fukuda, Y.: Global terrestrial carbon fluxes of 1999–2019 estimated by upscaling eddy covariance data with a random forest, Sci. Data, 7, 313, https://doi.org/10.1038/s41597-020-00653-5, 2020.

Zomer, R. J., Bossio, D. A., Sommer, R., and Verchot, L. V.: Global Sequestration Potential of Increased Organic Carbon in Cropland Soils, Sci. Rep., 7, 15554, https://doi.org/10.1038/s41598-017-15794-8, 2017.